Article

Neuron

The Raphe Dopamine System Controls the Expression of Incentive Memory

Graphical Abstract

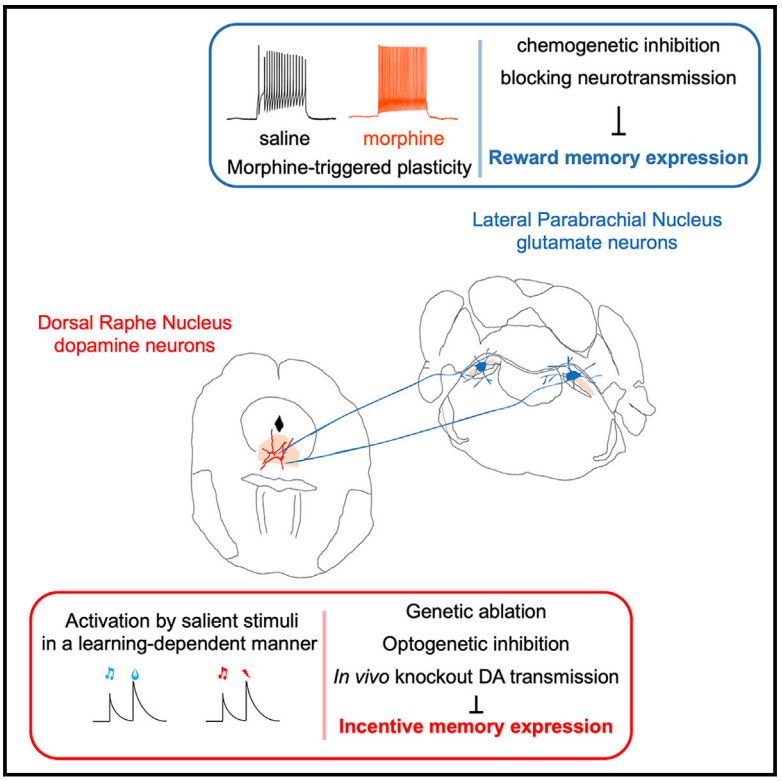

Highlights

- DRN dopamine neurons respond to salient stimuli in a learning-dependent manner
- DRN dopamine neurons are critical for the expression of incentive memory
- Morphine strengthens a glutamatergic input from the LPB to DRN DA neurons
- The glutamatergic LPB-to-DRN pathway controls reward memory expression

Authors

Rui Lin, Jingwen Liang, Ruiyu Wang, ..., Anan Li, Hui Gong, Minmin Luo

Correspondence

linrui@nibs.ac.cn (R.L.), luominmin@nibs.ac.cn (M.L.)

In Brief

A dopamine subsystem in the dorsal raphe controls the expression of incentive memory under normal conditions and in opioid addiction, with its glutamatergic input from the lateral parabrachial nucleus particularly important for reward memory expression.

Lin et al., 2020, Neuron *106*, 1–17
May 6, 2020
https://doi.org/10.1016/j.neuron.2020.02.009

CellPress

Please cite this article in press as: Lin et al., The Raphe Dopamine System Controls the Expression of Incentive Memory, Neuron (2020), https://doi.org/10.1016/j.neuron.2020.02.009

Neuron
Article

CellPress

The Raphe Dopamine System Controls the Expression of Incentive Memory

Rui Lin,[1,9,*] Jingwen Liang,[1,2,9] Ruiyu Wang,[1,3] Ting Yan,[1,4] Youtong Zhou,[1,5] Yang Liu,[1,4] Qiru Feng,[1,4] Fangmiao Sun,[3] Yulong Li,[3] Anan Li,[6,7,8] Hui Gong,[6,7,8] and Minmin Luo[1,2,4,5,10,*]
[1]National Institute of Biological Sciences (NIBS), Beijing 102206, China
[2]Graduate School of Peking Union Medical College, Chinese Academy of Medical Sciences, Beijing 100730, China
[3]School of Life Sciences, Peking University, Beijing 100871, China
[4]School of Life Sciences, Tsinghua University, Beijing 100084, China
[5]Chinese Institute for Brain Research, Beijing 102206, China
[6]Britton Chance Center for Biomedical Photonics, Wuhan National Laboratory for Optoelectronics-Huazhong University of Science and Technology, Wuhan 430074, China
[7]MoE Key Laboratory for Biomedical Photonics, School of Engineering Sciences, Huazhong University of Science and Technology, Wuhan 430074, China
[8]HUST-Suzhou Institute for Brainsmatics, JITRI Institute for Brainsmatics, Suzhou 215100, China
[9]These authors contributed equally
[10]Lead Contact
*Correspondence: linrui@nibs.ac.cn (R.L.), luominmin@nibs.ac.cn (M.L.)
https://doi.org/10.1016/j.neuron.2020.02.009

SUMMARY

The brain dopamine (DA) system participates in forming and expressing memory. Despite a well-established role of DA neurons in the ventral tegmental area in memory formation, the exact DA circuits that control memory expression remain unclear. Here, we show that DA neurons in the dorsal raphe nucleus (DRN) and their medulla input control the expression of incentive memory. DRN DA neurons are activated by both rewarding and aversive stimuli in a learning-dependent manner and exhibit elevated activity during memory recall. Disrupting their physiological activity or DA synthesis blocks the expression of natural appetitive and aversive memories as well as drug memories associated with opioids. Moreover, a glutamatergic pathway from the lateral parabrachial nucleus to the DRN selectively regulates the expression of reward memories associated with opioids or foods. Our study reveals a specialized DA subsystem important for memory expression and suggests new targets for interventions against opioid addiction.

INTRODUCTION

Memories of incentive stimuli that are either rewarding or aversive guide future behavioral choices, and their proper formation and expression are essential for animals' survival. Memory formation and expression are controlled by a distributed network that consists of multiple cortical and subcortical areas including the frontal cortex (Buckner et al., 1999; Preston and Eichenbaum, 2013), the hippocampus (Scoville and Milner, 1957; Squire, 1986), the striatum (Packard and Knowlton, 2002), and the amygdala (McGaugh et al., 1996; Ehrlich et al., 2009). These brain areas are subject to the regulation by the neuromodulatory systems, for example, the dopamine (DA) system. In both invertebrates and vertebrates, DA fundamentally contributes to memory formation (Lisman and Grace, 2005; Aso and Rubin, 2016; Kaun and Rothenfluh, 2017). In mammals, DA neurons in the ventral tegmental area (VTA) of the midbrain are important for appetitive associative learning and the formation of reward memories (Schultz et al., 1997; Wise, 2004; Keiflin and Janak, 2015). It remains unclear whether the VTA DA population and/or other DA populations outside the VTA are involved in memory expression.

Drugs of abuse often engage the neural pathways for learning and memory, through which stimuli, including environmental contexts and animals' internal states, are conditioned with the rewarding effects of drug intake and the withdrawal-induced aversive states to form addiction memories (Ungless et al., 2001; Nestler, 2001; Hyman, 2005; Wise and Koob, 2014; Lüscher, 2016). These pathological memories drive continuous drug seeking and render patients vulnerable to relapse (Hyman, 2005; Hyman et al., 2006). Addictive drugs—for example, opioids—hijack VTA DA neurons to mediate the initial behavioral reinforcement and the formation of opioid-related memories (Johnson and North, 1992). Multiple brain structures, including the central amygdala (CeA) (Zarrindast et al., 2003; Zimmerman et al., 2007; Cai et al., 2013; Li, 2019), the bed nucleus of the stria terminalis (BNST) (Avery et al., 2016; Stamatakis et al., 2014; Vranjkovic et al., 2017), the nucleus accumbens (Robinson and Kolb, 1997; Blaiss and Janak, 2009; Li et al., 2011; Zhu et al., 2016), and the periventricular thalamus (Li et al., 2014; Zhu et al., 2016), participate in the expression of opioid drug memory. These areas receive substantial DAergic inputs, although the exact roles and detailed circuit mechanisms of the DA system in drug memory expression remain elusive.

Considerable anatomical and transcriptional heterogeneity exists in the brain DA system (Poulin et al., 2014, 2018; Tiklová

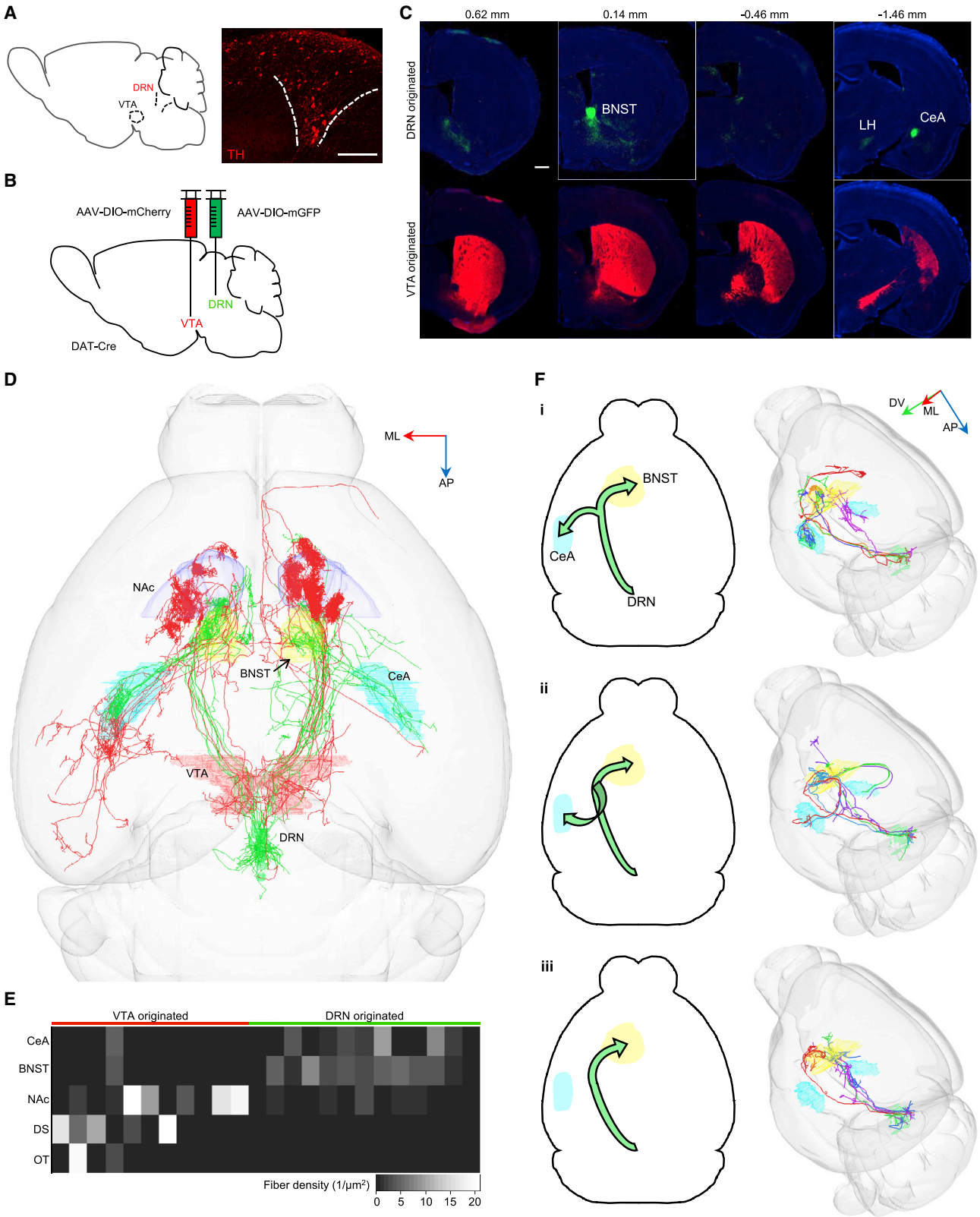

(legend on next page)

et al., 2019). Notably, the dorsal raphe nucleus (DRN) harbors a major extra-VTA DA population. Recent progress suggests these neurons' involvement in arousal (Cho et al., 2017), social interaction (Matthews et al., 2016), and fear response (Groessl et al., 2018). However, we know little about their potential functions in memory expression, especially the memories related to drug intake and withdrawal. Here, we use a combination of approaches, including whole-brain single-neuron reconstruction, fiber photometry, optogenetics, CRISPR/Cas9-mediated *in vivo* region-specific knockout, and rabies screening, to investigate the behavioral roles of DRN DA neurons in the expression of natural and drug memory. We found that the DRN DA population functions as an essential regulator of memory expression under normal conditions and in opioid addiction and further identified a brainstem input that is modified by opioid administration and is critical for the expression of reward memory. Collectively, these results establish a central role of DRN DA neurons in controlling memory expression and suggest potential targets for developing future intervention strategies against opioid addiction.

RESULTS

DRN DA Neurons Represent an Anatomically and Functionally Distinct DA Subsystem

DRN DA neurons were initially considered as the dorso-caudal extension of the VTA DA system (Hokfelt, 1984). Some recent studies suggest that DA neurons in the DRN and the VTA exhibit overlapping but biased projection patterns (Hasue and Shammah-Lagnado, 2002; Matthews et al., 2016; Cho et al., 2017). We first examined how DRN DA neurons are anatomically segregated from VTA DA neurons (Figure 1). We performed dual-color bulk tracing to compare the projection patterns between the DRN and the VTA DA populations (Figures 1A and 1B; Table S1 for specifics of vector injections). Unlike VTA DA neurons that predominantly project to the striatum and the frontal cortex (Ikemoto, 2007), DRN DA neurons project primarily to the CeA and the BNST in the extended amygdala (Figure 1C). To overcome the limitation of traditional bulk labeling (Hasue and Shammah-Lagnado, 2002), we further examine the projection patterns of DRN DA neurons with single-cell precision. We combined cell-type-specific sparse labeling and fluorescence micro-optical sectioning tomography (Lin et al., 2018) to reconstruct the complete morphologies of individual DRN DA neurons at the whole-brain level (Figures 1D and S1). Despite individual heterogeneity, DRN DA neurons showed dramatically different axonal projection pattern from VTA DA neurons (Figures 1D, 1E, and S1). All reconstructed DRN DA neurons innervate and form branching axonal terminals in the BNST (Figures 1E, 1F, and S1A). Based on the patterns of axonal projections to the CeA, we identified three projection types of DRN DA neurons. A majority (n = 9/13 reconstructed neurons) send axonal collaterals to the CeA, either through the external capsule (n = 4 cells; Figures 1Fi and S1) or via a ventral route (n = 5 cells; Figures 1Fii and S1A). The remaining 4 of the 13 reconstructed neurons do not project to the CeA (Figures 1Fiii and S1A). All of these neurons traversed their axons in the adjacent brain areas near the BNST, such as the nucleus accumbens, but did not form clear axonal terminals in these areas (Figures S1B and S1C). Together, our anatomical analyses demonstrate that DRN DA neurons are anatomically separated with VTA DA neurons and represent a distinct midbrain DA system.

We then investigated the physiological responses of DRN DA neurons toward various stimuli using fiber photometry of Ca^{2+} signals (Figure 2A). Contrary to VTA DA neurons that are activated mainly by rewards at the populational level (Cohen et al., 2012; Zhong et al., 2017), DRN DA neurons were activated by both rewarding stimuli (e.g., high-fat food [HFF] pellets, sucrose, and initial social encounter) and aversive stimuli (e.g., electric foot shock) (Figures 2B, 2C, and S2) (Matthews et al., 2016; Cho et al., 2017; Groessl et al., 2018). The strength of reward response of DRN DA neurons depended on animal hunger state and reward size (Figures S2A–S2I). Notably, learning induces excitatory responses of DRN DA neurons to the previously neutral cues. In the appetitive Pavlovian conditioning task that coupled a neutral auditory cue with delayed intraoral delivery of a sucrose solution (Figure S2J), DRN DA neurons showed gradually increasing responses toward the initially ineffective cue (Figures 2B and S2K–S2M). The Ca^{2+} signals associated with sucrose infusion did not exhibit the prediction error-like decreases seen with VTA DA neurons (Zhong et al., 2017) but remained rather stable throughout all training sessions (Figures S2K and S2N).

We observed similar learning effects on the response pattern of DRN DA neurons in a Pavlovian aversive conditioning test. Coupling a brief auditory cue with a delayed foot shock led to strong excitatory responses to both cue and foot shock (Figures 2C and S2O). On the following day when we repetitively presented the cue but omitted the foot shock, the cue-evoked response was initially strong and then gradually decreased, resulting in a smaller but significant response after 20 extinction trials (Figures S2P–S2R). Thus, the *in vivo* fiber photometry suggests that DRN and VTA DA neurons are functionally segregated. Although VTA DA neurons are mainly important for processing reward signals (Keiflin and Janak, 2015), DRN DA neurons may contribute to the learning and memory-associated behavioral processes related to both reward and aversion.

Figure 1. Dorsal Raphe Dopamine Neurons Represent an Anatomically Distinct DA Population

(A) Distribution of DRN DA neurons. Red: tyrosine hydroxylase (TH) immunoreactivity. VTA, ventral tegmental area.

(B) Schematic showing virus injection for dual-color anterograde tracing of DA neurons in the VTA (red) and in the DRN (green).

(C) Serial coronal sections showing the axonal projections of DRN (top) and VTA (bottom) DA neurons. Numbers above the images indicate the distance from the bregma. BNST, bed nucleus of the stria terminalis; LH, lateral hypothalamus; CeA, central amygdala.

(D) Reconstructions of 13 sparsely labeled single DRN DA (green) neurons and 11 VTA DA (red) neurons, registered to the Allen Institute common coordinate framework. NAc, nucleus accumbens.

(E) Fiber density heatmap of individual DRN DA and VTA DA neurons in major downstream target brain areas. DS, dorsal striatum; OT, olfactory tubercle.

(F) Schematic summaries of three DRN DA neuron projection types (left panel) and corresponding single neuron reconstructions registered to the Allen common coordinate framework (right panel). Each color represents one reconstructed neuron.

Scale bars, 200 μm (A) and 500 μm (C). See also Figure S1.

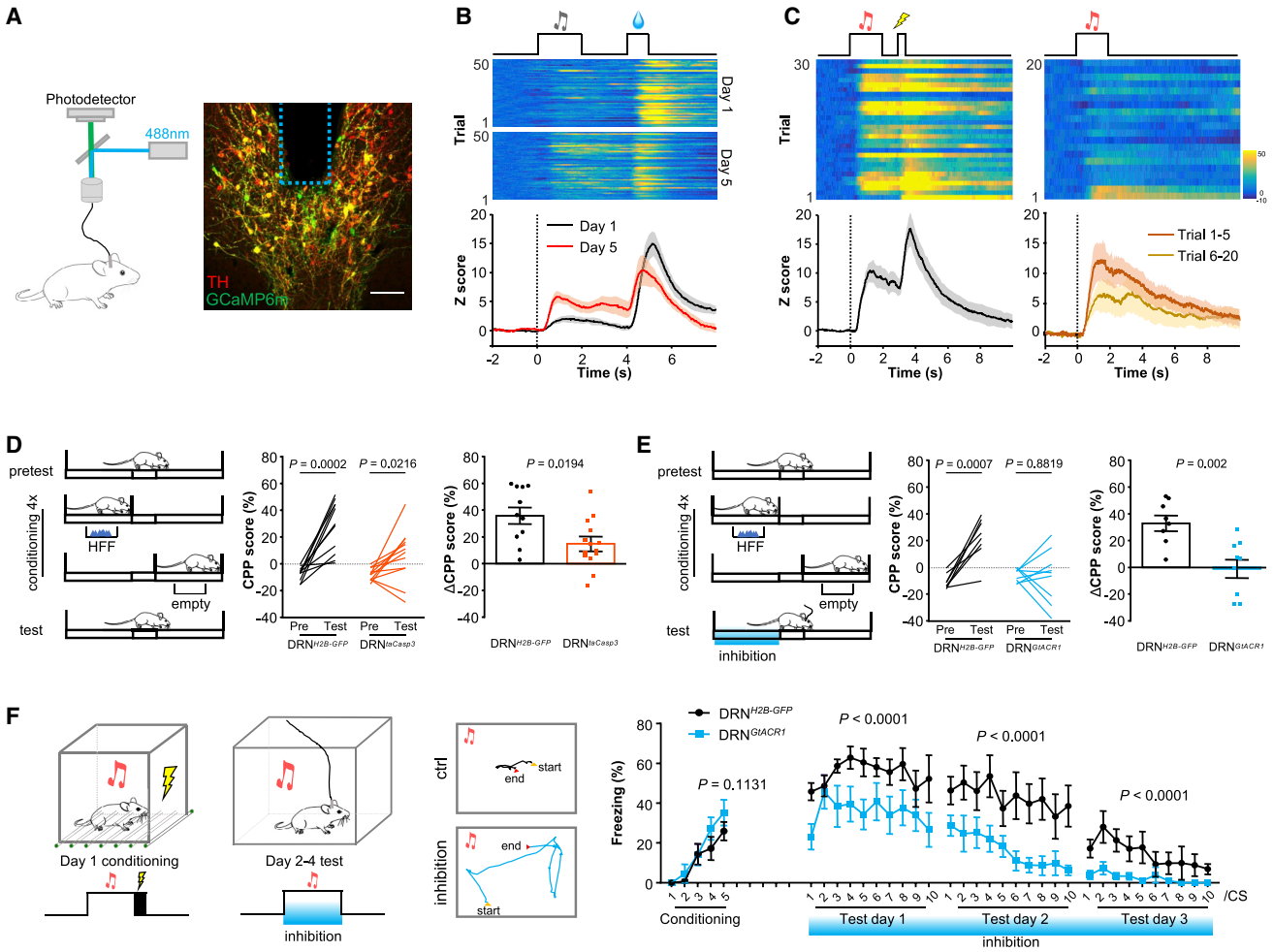

Figure 2. Dorsal Raphe Dopamine Neurons Are Essential for the Expression of Both Reward and Fear Memory

(A) Schematic of fiber photometry of Ca^{2+} signals (left). The right panel shows the specific expression of GCaMP6m (green) in tyrosine hydroxylase-immunopositive DRN DA neurons (red). Dashed lines indicate optic fiber placement.

(B) Heatmaps illustrating the Ca^{2+} signal changes (top, *Z* score), and peri-event plots (bottom) of the average Ca^{2+} signals of DRN DA neurons in the first and the fifth daily Pavlovian conditioning sessions that coupled an auditory cue with intra-oral infusion of sucrose solution (n = 5 mice).

(C) Heatmaps illustrating the Ca^{2+} signal changes (top, *Z* score), and peri-event plots (bottom) of the average Ca^{2+} signals of DRN DA neurons during tone-foot shock conditioning (left) and extinction (right) (n = 7 mice).

(D) The effect of ablating DRN DA neurons on HFF-conditioned place preference (CPP) (n = 11 $DRN^{H2B\text{-}GFP}$ mice in the ctrl group and 12 $DRN^{taCasp3}$ mice in the lesion group).

(E) The effect of optogenetically inhibiting DRN DA neurons during the test phase on HFF CPP (n = 8 $DRN^{H2B\text{-}GFP}$ mice in the ctrl group and 9 DRN^{GtACR1} mice in the inhibition group).

(F) The effect of optogenetically inhibiting DRN DA neurons in the test phase on mice's freezing response in the fear conditioning test (two-way ANOVA; n = 9 $DRN^{H2B\text{-}GFP}$ mice in the ctrl group and 7 DRN^{GtACR1} mice in the inhibition group). Left: behavior paradigm; middle: representative locomotion traces of mice in the first trial of the first test session.

See Table S2 for detailed statistical tests. p values are shown in the graph. Data are means ± SEM. Scale bars, 100 μm. See also Figures S2 and S3.

DRN DA Neurons Control the Expression of Incentive Memory

Given that both rewarding and aversive stimuli, as well as their predicting cues, activate DRN DA neurons, we asked whether and how DRN DA neurons participate in the formation and/or expression of incentive memory. We first used a classic conditioned place preference (CPP) test as a behavioral paradigm for measuring reward memory. In a three-chamber apparatus, food-restricted mice acquired preference to the side chamber that was conditioned with HFF pellets hidden beneath the floor but not to the remaining side chamber that was conditioned with an empty dish beneath the floor. We selectively killed DRN DA neurons by injecting AAV-FLEX-taCasp3-TEVp (Yang et al., 2013) into the DRN of DAT-Cre mice before the CPP assay (Figures S3A and S3B). Ablating DRN DA neurons significantly decreased HFF-induced CPP (Figure 2D) but did not affect

animals' preference for the HFF or animals' locomotion (Figures S3C–S3G), thereby indicating that the detrimental effects of ablating DRN DA neurons correspond to an impairment in reward memory.

To differentiate the functions of DRN DA neurons in the formation and expression of reward memory, we used the light-sensitive chloride channel, GtACR1 (Govorunova et al., 2015), to optogenetically inhibit DRN DA neurons in different phases of the HFF-induced CPP test (Figures S3H–S3J). Inhibiting DRN DA neurons during the conditioning phase did not alter HFF-induced CPP (Figure S3K), suggesting that DRN DA neurons are dispensable for the formation of reward memory. In contrast, inhibiting DRN DA neurons during the test phase significantly reduced the time that mice spent in the HFF-paired side (Figure 2E). Neither optogenetic inhibition nor activation led to avoidance behavior toward the light-paired chamber in a real-time place aversion (RTPA) test (Figures S3L and S3M), which suggested that the decreased performance in HFF-induced CPP was indeed due to the impaired memory expression rather than a change in affective state. Moreover, robust expression of Fos, a marker of neuronal activity, was induced in DRN DA neurons in the test phase of the HFF-induced CPP test (Figure S3N), indicating that DRN DA neurons are activated during reward memory expression. Therefore, these results demonstrate that DRN DA neurons specifically control the expression of reward memory.

We tested whether DRN DA neurons would also be required for the formation and/or expression of aversive memory. In the fear conditioning test, genetic ablation of DRN DA neurons significantly reduced freezing responses in the extinction phase (Figures S3O and S3P) without affecting locomotion or pain sensations in the mice (Figures S3Q–S3S), demonstrating that the ablation of DRN DA neurons affects aversive memory. We then used GtACR1 to selectively inhibit DRN DA neurons in the conditioning or extinction phase of the fear conditioning test. Following optogenetic inhibition in the conditioning phase, we observed a statistically significant effect of the interaction between treatment and time on the freezing duration (Figures S3U) but not on the total freezing duration between test and control groups (Figure S3T). Interestingly, optogenetic inhibition in the test phase resulted in a clear decrease in animals' freezing response (Figures 2F and S3V), suggesting that DRN DA neurons play a more prominent function in the expression than in the formation of aversive memory.

DA Neurons in the DRN and the VTA, Respectively, Control the Expression and the Formation of Opioid Reward Memory

On the basis of our anatomical tracing, recording, and behavioral data, we propose that DRN DA neurons represent a distinct midbrain DA system—parallel to the VTA DA system—that functions discretely to regulate the expression of incentive memory associated with either rewarding or aversive stimuli. Since both the DA system and the DRN have been implicated in opioid addiction (Mansour et al., 1995), we hypothesized that DRN DA neurons may participate in the development and/or maintenance of opioid-related drug memory. To test this, we used the classic morphine-induced CPP test.

We examined the activity of DRN DA neurons in the morphine-induced CPP test. In the conditioning phase, acute morphine administration did not change Fos expression in the DRN DA neurons (Figures 3A, 3B, and S4A). However, in the test phase, we observed significantly stronger Fos signals in DRN DA neurons in the morphine-paired chamber than in the saline-paired chamber (Figures 3A and 3B). These findings were recapitulated by fiber photometry of DRN DA neurons in the same behavior paradigm: in the test phase, DRN DA neurons showed higher activity when mice were confined in the morphine-paired chamber than in the saline-paired chamber (Figure S4B). The increase in population Ca^{2+} signals as revealed by fiber photometry appears less striking than that in Fos immunosignals, possibly because of the limitation of using averaged metrics for fiber photometry. More importantly, in the conditioning phase, the activity of DRN DA neurons was lower when mice were confined in the morphine-paired chamber than in the saline-paired chamber (Figure S4C). These results collectively indicate that the expression but not the formation of opioid-related drug memory involves DRN DA neurons.

We used genetic ablation and optogenetic inhibition to investigate whether the formation and/or expression of drug memory requires DRN DA neurons. Ablating DRN DA neurons significantly reduced morphine-induced CPP (Figure 3C). Consistent with the activation of DRN DA neurons during drug memory expression, optogenetically inhibiting these neurons in the test phase completely blocked the expression of morphine-induced CPP (Figure 3E). However, such inhibition in the conditioning phase did not affect morphine-induced CPP (Figures 3D and S4D). To test whether inhibiting DRN DA neurons in one session could have long-lasting effects in the following sessions, we performed an additional morphine-induced CPP test, in which the test phase was extended to five consecutive daily sessions and DRN DA neurons were silenced only in the second test session. Inhibiting DRN DA neurons significantly reduced morphine-induced CPP in the second test session but did not affect animals' performances in the following test sessions (Figure S4E). Moreover, optogenetically activating DRN DA neurons in the conditioning phases did not affect morphine-induced CPP (Figure S4F), suggesting the acute inhibition by morphine does not contribute to the formation of drug memory. These results together demonstrate that DRN DA neurons regulate the expression but neither the formation nor reconsolidation of opioid reward memory.

To directly compare the role of DRN and that of VTA DA neurons in opioid-related drug memory, we examined the activities of VTA DA neurons in the same morphine-induced CPP test. In the conditioning phase, morphine administration resulted in strong Fos expression in VTA DA neurons, confirming that morphine acutely activates VTA DA neurons (Figures S4G and S4H) (Wei et al., 2018). In the expression phase, VTA DA neurons showed only slightly higher Fos expression in the morphine-paired chamber than in the saline-paired chamber (Figures S4G and S4H). Moreover, the activation of VTA DA neurons in the morphine-paired chamber was much weaker in the expression phase than in the conditioning phase. Consistent with previous studies (Chen et al., 2015; Harris et al., 2004),

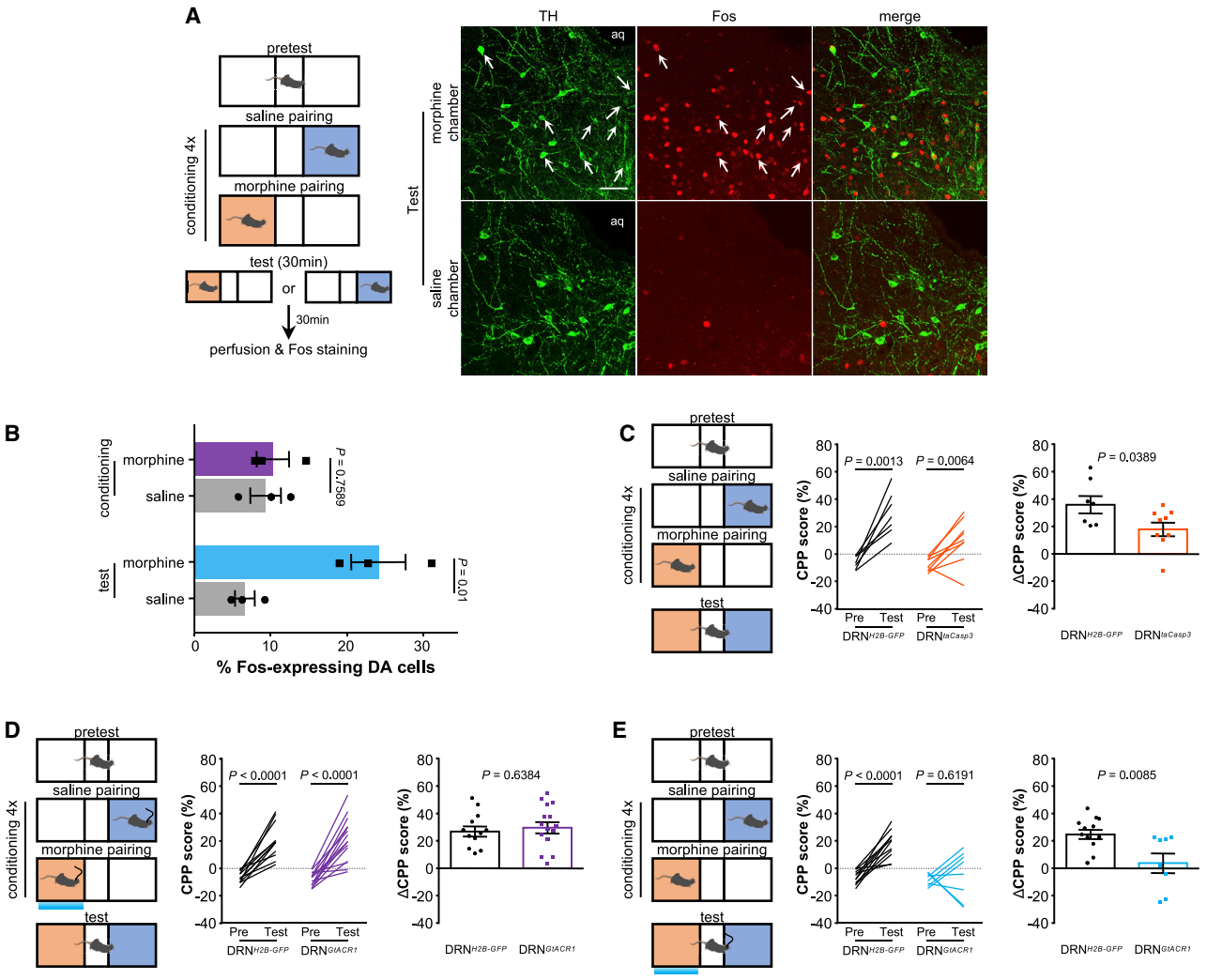

Figure 3. DRN DA Neurons Control the Expression of Morphine Reward Memory

(A) Fos expression patterns in the DRN of mice that underwent morphine conditioning and tested in the morphine-coupled chamber (top) or the saline-coupled chamber (bottom). Arrows point to Fos (red) and TH (green) dual-immunopositive cells.

(B) Quantification of Fos-expressing DA neurons in the DRN during the morphine conditioning phase or the test phase (two-sided unpaired t test; n = 3 mice for each group).

(C) The effect of ablating DRN DA neurons on morphine-induced CPP (n = 7 $DRN^{H2B\text{-}GFP}$ mice in the ctrl group and 9 $DRN^{taCasp3}$ mice in the lesion group).

(D) The effect of optogenetically inhibiting DRN DA neurons in the conditioning phase on morphine-induced CPP (n = 12 $DRN^{H2B\text{-}GFP}$ mice in the ctrl group and 15 DRN^{GtACR1} mice in the inhibition group).

(E) The effect of optogenetically inhibiting DRN DA neurons in the test phase on morphine-induced CPP (n = 12 $DRN^{H2B\text{-}GFP}$ mice in the ctrl group and 8 DRN^{GtACR1} mice in the inhibition group).

See Table S2 for detailed statistical tests. p values are shown in the graph. Data are means ± SEM. Scale bar, 50 μm. See also Figure S4.

selectively inhibiting VTA DA neurons in the conditioning phase dramatically decreased morphine-induced CPP (Figures S4I–S4K). Surprisingly, inhibiting VTA DA neurons in the expression phase did not affect morphine-induced CPP (Figure S4L). Thus, our results establish that DRN and VTA DA neurons control different phases of opioid-related drug memory. Specifically, DRN DA neurons are essential for the expression but not formation of drug memory. Conversely, VTA DA neurons play a more important role in the formation than in the expression of drug memory.

The Formation and the Expression of Opioid Withdrawal Memory Require DRN DA Neurons

Chronic use of opioids can lead to both physiological and psychological dependence, after which abrupt drug abstinence elicits unpleasant withdrawal symptoms. We investigated whether the development and expression of opioid withdrawal also involves DRN DA neurons. We first carried out a spontaneous opioid withdrawal-induced conditioned place aversion (CPA) test (Bechara et al., 1995; Zhu et al., 2016). In the initial conditioning session, Fos expression in DRN DA neurons was

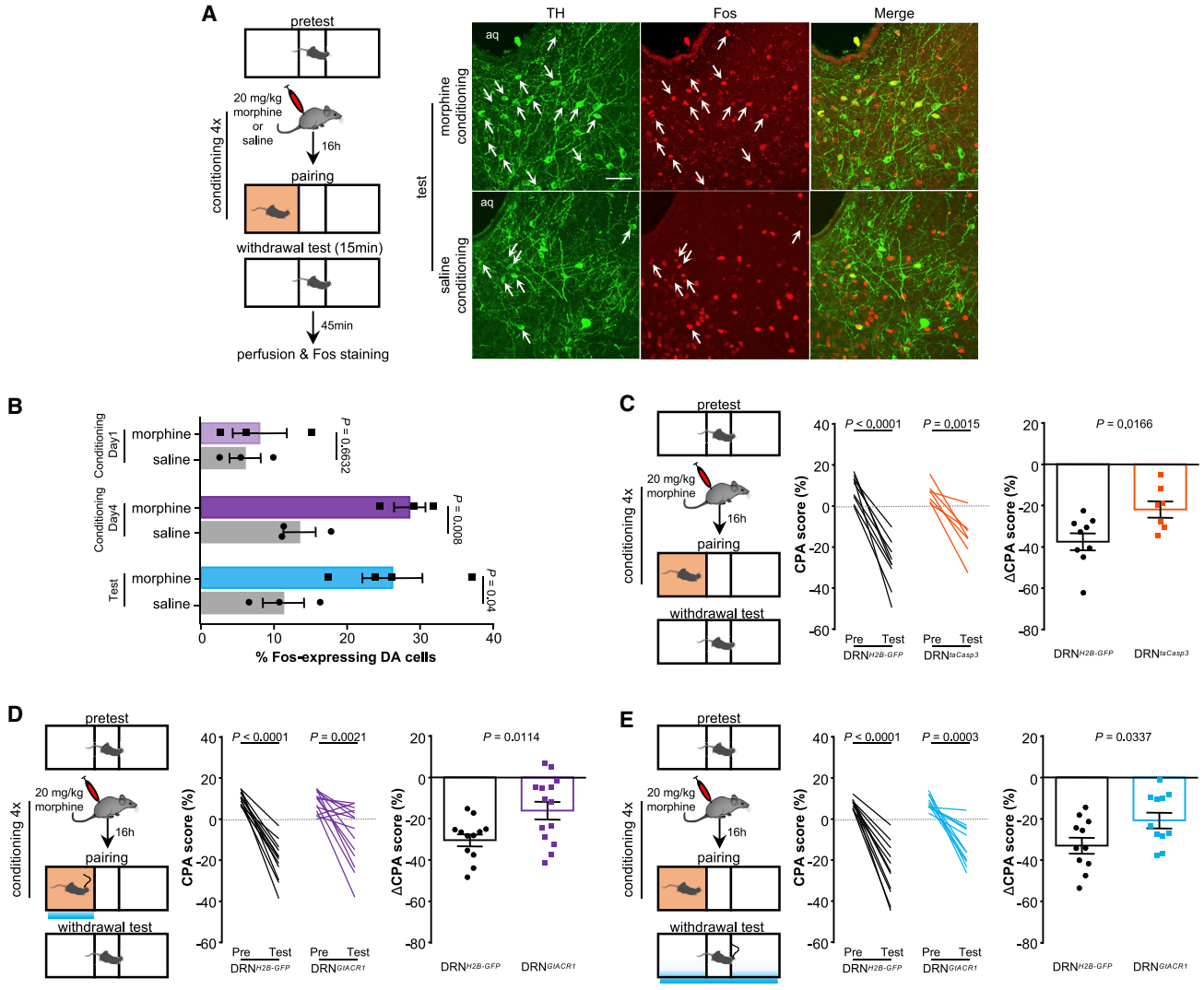

Figure 4. The Formation and the Expression of Morphine Withdrawal Memory Require DRN DA Neurons

(A) Fos expression patterns of DRN DA neurons during the test phase of the spontaneous morphine withdrawal-induced conditioned place aversion (CPA) test. Arrows point to Fos (red) and TH (green) dual-immunopositive cells. Saline conditioning served as control.

(B) Quantification of Fos-expressing DRN DA neurons during the spontaneous morphine withdrawal-induced CPA test (two-sided unpaired t test; n = 3 mice for each group except for 4 mice for the morphine-injected test phase group).

(C) The effect of ablating DRN DA neurons on spontaneous morphine withdrawal-induced CPA (n = 9 $DRN^{H2B\text{-}GFP}$ mice in the ctrl group and 7 $DRN^{taCasp3}$ mice in the lesion group).

(D) The effect of optogenetically inhibiting DRN DA neurons in the conditioning phase on spontaneous opioid withdrawal-induced CPA (n = 12 $DRN^{H2B\text{-}GFP}$ mice in the ctrl group and 14 DRN^{GtACR1} mice in the inhibition group).

(E) The effect of optogenetically inhibiting DRN DA neurons in the test phase on spontaneous morphine withdrawal-induced CPA (n = 11 $DRN^{H2B\text{-}GFP}$ mice in the ctrl group and 11 DRN^{GtACR1} mice in the inhibition group).

See Table S2 for detailed statistical tests. p values are shown in the graph. Data are means ± SEM. Scale bars, 50 μm. See also Figure S5.

similar between morphine- and saline-injected groups (Figures 4B and S5A). In contrast, we observed higher Fos expression in DRN DA neurons in the morphine-injected mice in the fourth conditioning session as well as in the test phase (Figures 4A, 4B, and S5A). Consistent with the Fos expression mapping, fiber photometry revealed stronger Ca^{2+} signals in DRN DA neurons in the fourth conditioning session and in the test phase (Figures S5B and S5C).

We then ablated or inhibited DRN DA neurons and investigated whether this affected opioid withdrawal. The lesion of DRN DA neurons significantly reduced spontaneous opioid withdrawal-induced CPA (Figure 4C). Optogenetic inhibition of DRN DA neurons in both the conditioning and test phases decreased spontaneous opioid withdrawal induced CPA (Figures 4D and 4E).

Following opioid dependence, application of naloxone, a opioid receptor blocker, precipitates drug withdrawal and

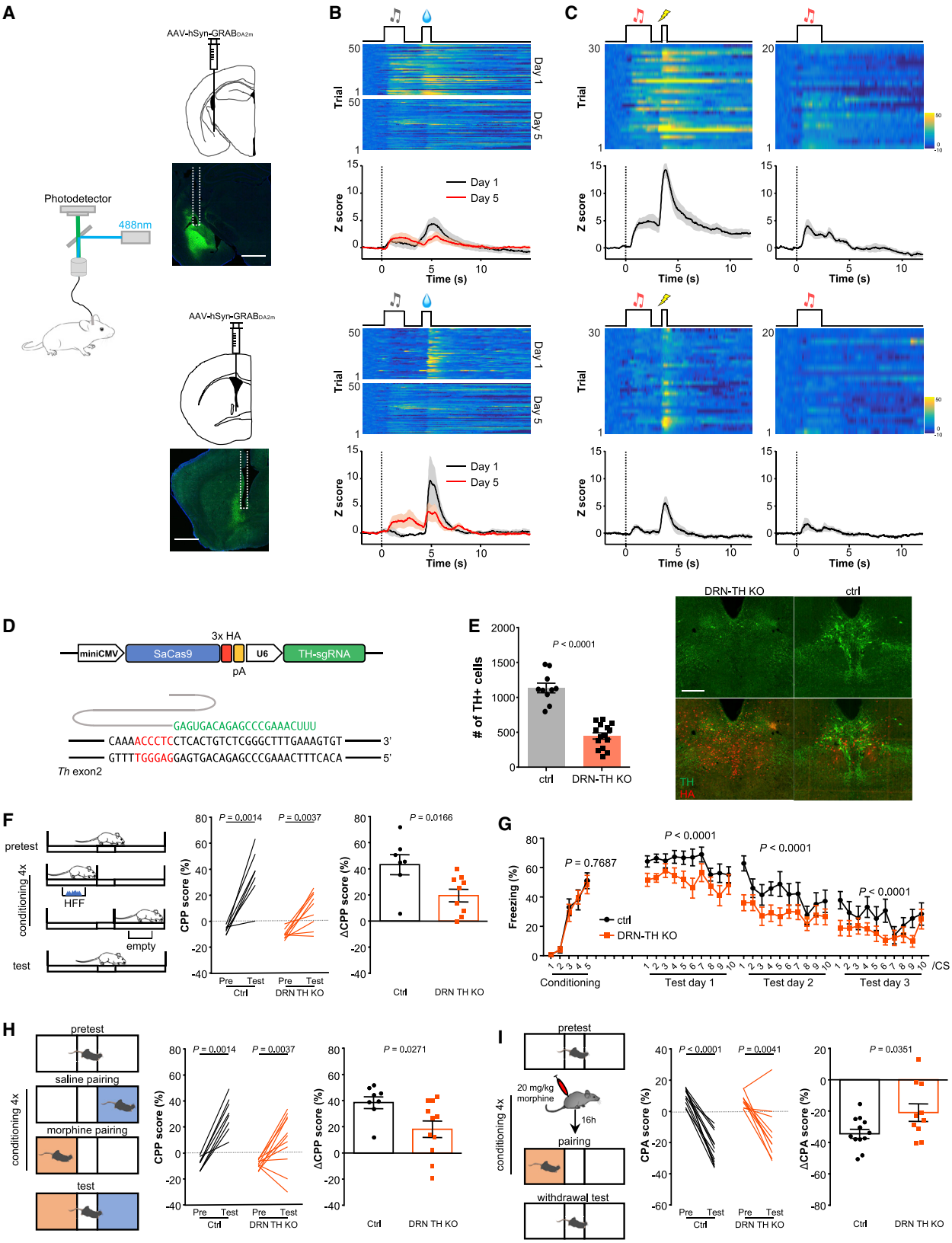

(legend on next page)

produces strong physical and psychological withdrawal symptoms (Zhu et al., 2016). We further examined the behavioral consequences of ablating DRN DA neurons in naloxone-induced withdrawal. Ablating DRN DA neurons reduced CPA (Figures S5D and S5E) but did not alleviate the physical withdrawal symptoms (Figures S5F–S5H). This suggests that ablating DRN DA neurons affects the "psychological" (aversive memory expression) but not the "physical" aspect of drug withdrawal. Thus, these results together establish that DRN DA neurons are indispensable for the expression of negative memories associated with opioid dependence.

DA from DRN DA Neurons Is Essential for Memory Expression

To investigate whether DRN DA neurons release DA to mediate their behavioral functions (Li et al., 2016a; Matthews et al., 2016), we first examined the DA transmission profiles in the major downstream targets of DRN DA neurons by using an optimized genetically encoded DA sensor, $GRAB_{DA2m}$ (unpublished data; Sun et al., 2018) (Figure 5A). We expressed $GRAB_{DA2m}$ in the CeA and the BNST and used fiber photometry to record the fluorescent signal changes in an appetitive Pavlovian conditioning test and the fear conditioning test (Figures 5B and 5C). Consistent with our fiber photometry of Ca^{2+} signals at DRN DA neurons' somata, the DA levels in both the CeA and the BNST showed transient increases toward sucrose, sucrose-predicting auditory cue, foot shock, and foot-shock-predicting auditory cue (Figures 5H, 5I, and S6). We next investigated whether memory expression requires DA transmission from DRN DA neurons. We used AAV-mediated CRISPR/Cas9 technology (Ran et al., 2015) *in vivo* to knock out tyrosine hydroxylase (TH), a rate-limiting enzyme for DA biosynthesis, in the DRN (Figure 5D). Compared with that of control single guide RNA (sgRNA), the expression of an AAV-SaCas9 vector bearing a sgRNA targeting the 2nd exon of *Th* effectively reduced the number of TH-expressing neurons in the DRN (Figure 5E). The loss of DA biosynthesis in the DRN significantly reduced HFF-induced CPP, freezing responses in the fear conditioning test, morphine-induced CPP, and spontaneous opioid withdrawal-induced CPA (Figures 5F–5I). Thus, these results suggest that the DA transmission from DRN DA neurons is essential for the expression of both reward and aversive memory associated with natural stimuli and opioids.

Morphine Administration Enhances a Glutamatergic Pathway from the LPB to DRN DA Neurons

We sought insight into the upstream circuit underlying the engagement of DRN DA neurons in opioid dependence. By adopting a recently developed strategy that screens for the drug-enhanced retrograde labeling (Beier et al., 2017), we used rabies virus (RV) retrograde tracing to identify the presynaptic inputs to DRN DA neurons and to examine any changes in these inputs upon morphine administration (Figure 6A). DRN DA neurons received inputs predominantly from subcortical areas, including the extended amygdala, hypothalamic areas, the lateral habenula, the VTA/substantia nigra, and the lateral parabrachial nucleus (LPB) (Figures 6B, S7B, and S7C). In general, the presynaptic inputs of DRN DA neurons were similar between saline- and morphine-injected groups (Figures 6B and S7B). Strikingly, only one upstream region—the LPB—showed proportionally increased input to DRN DA neurons (Figures 6B and 6C), indicating that morphine administration may trigger plasticity in the LPB-to-DRN DA pathway.

To further analyze this change, we employed an axon-terminal-transducing AAV (AAVretro) (Tervo et al., 2016) to drive gene expression specifically in DRN-projecting LPB neurons. Using a dual-AAV intersectional strategy (AAVretro-FLPo injection in the DRN and AAV-fDIO-ChR2-mCherry injection in the LPB), we expressed Channelrhodopsin-2 in DRN-projecting LPB neurons in DAT-Cre mice (Figure 6D, left). We also injected AAV-DIO-H2B-GFP in the DRN to label DRN DA neurons. In patch-clamp recordings of brain slices, optogenetically stimulating the axonal terminals of DRN-projecting LPB neurons evoked excitatory postsynaptic currents (EPSCs) in 84.4% of DRN DA neurons (27/32 cells recorded; Figure 6D, middle). Following the isolation of the light-evoked monosynaptic EPSCs using blockers for sodium channels and potassium channels (tetrodotoxin and 4-Aminopyridine), we found the EPSCs were reversibly antagonized by the selective AMPA-type glutamate

Figure 5. *In Vivo* Knockout of Dopamine Transmission in DRN DA Neurons Impairs the Expression of Natural and Addiction Memory

(A) Schematic of fiber photometry of DA transmission using a genetically encoded DA sensor ($GRAB_{DA2m}$). The right panel shows virus injection and optic fiber implantation in the CeA (top) and the BNST (bottom). Dashed lines indicate optic fiber placement.

(B) Heatmaps illustrating the DA signal changes and peri-event plots of the average DA signals in the CeA (top) and in the BNST (bottom) during the first and the fifth daily Pavlovian conditioning sessions that coupled an auditory cue with intra-oral infusion of sucrose solution (n = 8 recording sites in 6 mice for the CeA, and 4 recording sites in 4 mice for the BNST).

(C) Heatmaps illustrating the DA signal changes and peri-event plots of the average DA signals in the CeA (top) and in the BNST (bottom) during cue-foot shock conditioning (left) and extinction (right) (n = 6 recording sites in 5 mice for the CeA, and 5 recording sites in 5 mice for the BNST).

(D) The designs of AAV vector (top) and the sgRNA targeting the exon 2 of *Th* (bottom).

(E) The effect of SaCas9-mediated *in vivo* KO on the number of TH-positive neurons in the DRN (two-sided unpaired t test; n = 10 $DRN^{sgRNA\text{-}GFP}$ mice in the ctrl group and 15 $DRN^{sgRNA\text{-}TH}$ mice in the DRN-TH KO group). The right panel shows confocal images of the DRN in mouse brain sections immunostained against TH (green) and the HA tag on SaCas9 (red).

(F) The effect of knocking out TH in the DRN on HFF CPP (n = 7 $DRN^{sgRNA\text{-}GFP}$ mice in the ctrl group and 9 $DRN^{sgRNA\text{-}TH}$ mice in the DRN-TH KO group).

(G) The effect of knocking out TH in the DRN on mice's freezing response in the fear conditioning test (two-way ANOVA; n = 12 $DRN^{sgRNA\text{-}GFP}$ mice in the ctrl group and 14 $DRN^{sgRNA\text{-}TH}$ mice in the DRN-TH KO group).

(H) The effect of knocking out TH in the DRN on morphine-induced CPP (n = 8 $DRN^{sgRNA\text{-}GFP}$ mice in the ctrl group and 11 $DRN^{sgRNA\text{-}TH}$ mice in the DRN-TH KO group).

(I) The effect of knocking out TH in the DRN on spontaneous morphine withdrawal-induced CPA (n = 12 $DRN^{sgRNA\text{-}GFP}$ mice in the ctrl group and 10 $DRN^{sgRNA\text{-}TH}$ mice in the DRN-TH KO group).

See Table S2 for detailed statistical tests. p values are shown in the graph. Data are means ± SEM. Scale bars, 1 mm (A) and 100 μm (E). See also Figure S6.

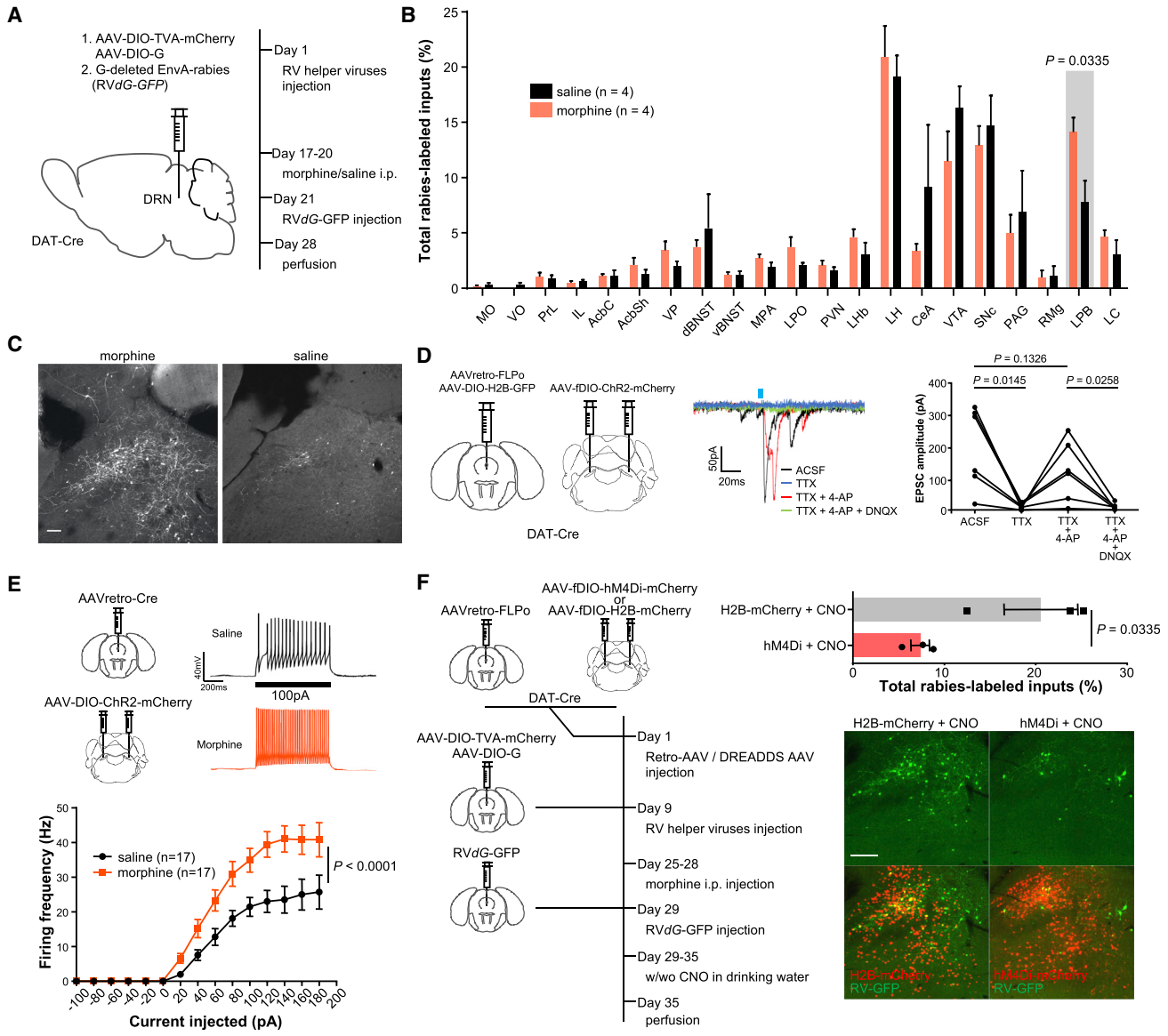

Figure 6. A Rabies Screen Identified a Glutamatergic Lateral Parabrachial Nucleus-to-DRN DA Neuron Pathway that Is Enhanced after Morphine Administration

(A) Experimental timeline for the rabies screen of inputs to DRN DA neurons.

(B) Rabies-labeled inputs to DRN DA neurons in morphine- and saline-injected mice (two-sided t test corrected for multiple comparisons using the Holm-Sidak method; only the highlighted comparison reached statistical significance; n = 4 mice for each group).

(C) Confocal images showing rabies-labeled neurons in the LPB in morphine- and saline-injected mice.

(D) The effect of optogenetically stimulating the axon terminals of LPB neurons in the DRN on DRN DA neurons (two-sided paired t test; n = 6 cells). Left: schematic of virus injection. Middle: example traces of a recorded DRN DA neurons. ACSF, artificial cerebrospinal fluid; TTX, tetrodotoxin; 4-AP, 4-Aminopyridine; DNQX, 6,7-dinitroquinoxaline-2,3-dione.

(E) Slice recording of DRN-projecting LPB neurons in saline- and morphine-injected mice. Left: schematic of virus injection. Middle: example traces from recorded DRN-projecting LPB neurons in saline- and morphine-injected mice. Right: frequency of action potentials over the range of current steps (two-way ANOVA; n = 17 cells for both saline- and morphine-injected mice).

(F) The effect of silencing DRN-projecting LPB neurons on rabies labeled inputs from the LPB to DRN DA neurons after morphine administration. Left: experimental timeline. Right top: quantification of rabies labeled neurons in the LPB in ctrl and CNO-treated mice (two-sided unpaired t test; n = 3 mice for each group). Right bottom: confocal images showing rabies-labeled neurons in the LPB in ctrl and CNO-treated mice.

See Table S2 for detailed statistical tests. p values are shown in the graph. Data are means ± SEM. Scale bars, 100 μm (C and F). See also Figure S7.

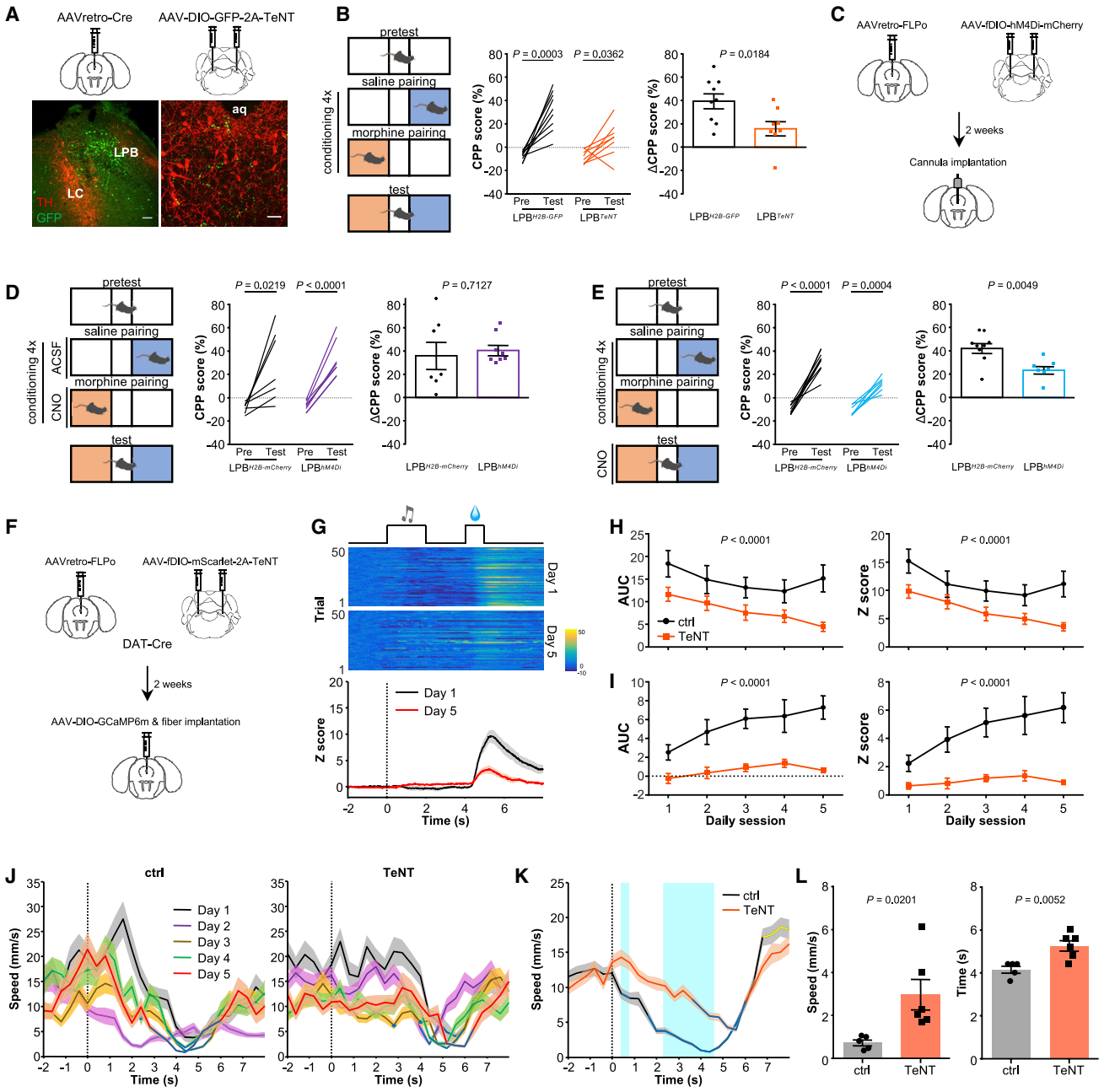

Figure 7. Silencing the LPB-to-DRN DA Neuron Pathway Disrupts the Reward Processing by DRN DA Neurons and Impairs the Expression of Reward Memory

(A) Dual-AAV strategy for specifically blocking the neurotransmission of DRN-projecting LPB neurons. TeNT, tetanus toxin.

(B) The effects of blocking the neurotransmission of DRN-projecting LPB neurons on morphine-induced CPP (n = 9 $LPB^{H2B\text{-}GFP}$ mice in the ctrl group and 8 LPB^{TeNT} mice in the TeNT group).

(C) Schematic of virus injection and cannula implantation for inhibiting axon terminals of DRN-projecting LPB neurons in the DRN.

(D and E) The effect of inhibiting axon terminals of DRN-projecting LPB neurons in the DRN (D) in the conditioning phase (n = 7 $DRN^{H2B\text{-}mCherry}$ mice in the control group and 8 DRN^{hM4Di} mice in the inhibition group) and (E) in the test phase on morphine-induced CPP (n = 9 $DRN^{H2B\text{-}mCherry}$ mice in the control group and 7 DRN^{hM4Di} mice in the inhibition group).

(F) Schematic of virus injection and fiber implantation for blocking the neurotransmission of DRN-projecting LPB neurons and fiber recording of DRN DA neurons.

(G) Heatmaps illustrating the Ca^{2+} signal changes (top, *Z* score), and peri-event plots (bottom) of the average Ca^{2+} signals of DRN DA neurons in the first and the fifth daily Pavlovian conditioning sessions that coupled an auditory cue with intra-oral infusion of sucrose solution (n = 6 mice). The neurotransmission of DRN-projecting LPB neurons in the recorded mice was blocked as shown in (F).

(legend continued on next page)

receptor antagonist (6,7-dinitroquinoxaline-2,3-dione), demonstrating that DRN DA neurons receive monosynaptic glutamatergic inputs from LPB neurons (Figure 6D, right). Consistently, further anatomical analysis confirmed the glutamatergic nature of this LPB-to-DRN pathway, as only ~5% of DRN-projecting LPB neurons are GABAergic (Figure S7D). We used the same strategy to map the connectivity between DRN-projecting LPB neurons and other two major DRN cell types, DRN serotonin neurons, and DRN GABAergic neurons (Figures S7E and S7F). We observed small monosynaptic glutamatergic currents from only 41.7% of DRN serotonin neurons (5/12 cells recorded) and 21.4% of DRN GABAergic neurons (3/14 cells recorded) (Figures S7E and S7F). Thus, DRN-projecting LPB neurons preferentially target DRN DA neurons among the three major cell types in the DRN (Figure S7G).

By examining data from patch-clamp recordings of brain slices that were prepared from mice after receiving daily i.p. injections of saline or morphine over four consecutive days, we discovered that DRN-projecting LPB neurons were more excitable in morphine-injected mice than in saline-injected mice (Figure 6E). To investigate whether the morphine-induced increase of LPB inputs to DRN DA neurons results from the observed enhancement in excitability of DRN-projecting LPB neurons induced by morphine administration, we performed an additional RV tracing in which we used inhibitory designer receptor exclusively activated by designer drugs (DREADD) hM4Di (Armbruster et al., 2007) to silence DRN-projecting LPB neurons after RV injection (Figure 6F, left). Silencing DRN-projecting LPB neurons completely reversed the increase in the number of RV-labeled LPB neurons induced by morphine administration (Figure 6F, right). These results therefore demonstrate that morphine administration causes an increase of glutamatergic inputs from the LPB to DRN DA neurons and show that this increase is mediated by the morphine-induced enhancement of LPB neuron excitability.

The LPB-to-DRN Pathway Is Essential for Reward Memory Expression

The LPB participates several physiological and behavioral processes related to sensory processing and behavioral homeostasis and may be modulated by opioid receptor activity (Colombari et al., 1996; Geerling and Loewy, 2007; De Araujo, 2009; Wu et al., 2009, 2012; Suzuki et al., 2012; Jarvie and Palmiter, 2017; Ryan et al., 2017; Kaur et al., 2017; Palmiter, 2018). However, its function in memory expression and addiction remains largely unexplored. To determine the functional relevance of the LPB-to-DRN pathway, we expressed tetanus neurotoxin (TeNT) selectively in DRN-projecting LPB neurons, again by a dual-AAV intersectional strategy (AAVretro-Cre injection in the DRN and AAV-DIO-GFP-2A-TeNT injection in the LPB), to block their neurotransmission (Figures 7A and S8). This manipulation significantly reduced morphine-induced CPP (Figure 7B). We further expressed the inhibitory DREADD hM4Di in DRN-projecting LPB neurons and locally infused clozapine-N-oxide (CNO) within the DRN to selectively inhibit the synaptic transmission of these neurons in the DRN. Inhibiting this pathway in the conditioning phase of the morphine-induced test did not cause significant changes in morphine-induced CPP (Figures 7C and 7D). Such inhibition in the test phase, however, resulted in large reduction in morphine-induced CPP (Figure 7E), suggesting that the LPB-to-DRN pathway is required for the expression but not the formation of opioid reward memory. In contrast, blocking the neurotransmission of DRN-projecting LPB neurons did not affect the animals' behaviors in two behavior models of opioid withdrawal (Figures S9A and S9B) and did not alleviate physical withdrawal symptoms (Figures S9C–S9E). These results indicate that DRN-projecting LPB neurons selectively regulate the positive but not negative aspects of opioid drug memory.

We next investigated whether DRN-projecting LPB neurons distinctly contribute to reward and aversion processing. Similar to the effects we observed for morphine-induced CPP, blocking the neurotransmission of DRN-projecting LPB neurons also decreased HFF-induced CPP (Figure S9F), without affecting animals' food intake or locomotion (Figures S9G–S9K). We observed higher Fos expression in DRN-projecting LPB neurons in the test phase (Figure S9N), suggesting the engagement of these neurons in the expression of natural reward memory. In addition, this blockade did not affect animals' freezing responses in the fear conditioning test (Figures S9L and S9M). Consistently, DRN-projecting LPB neurons were not activated by foot shock (Figure S9N). These results thus indicate that that DRN-projecting LPB neurons selectively regulate reward processing.

Finally, we examined the effects of blocking the neurotransmission of DRN-projecting LPB neurons on the physiological responses of DRN DA neurons to reward and its predicting cue. We expressed Ca^{2+} sensors in DRN DA neurons by infusing AAV-DIO-GCaMP6m into the DRN of DAT-Cre mice. We further expressed TeNT in DRN-projecting LPB neurons by infusing AAVretro-FLPo in the DRN and the flippase-dependent AAV-fDIO-mScarlet-2A-TeNT in the LPB. We then used fiber

(H) The AUC (left) and peak *Z* score (right) of the average response to the sucrose delivery (4–6 s) across five daily classic conditioning sessions (two-way ANOVA; n = 5 mice in the ctrl group and 6 mice in the TeNT group).

(I) The area under curve (AUC; left) and peak *Z* score (right) of the average response to the cue presentation (0–2 s) across five daily conditioning sessions (two-way ANOVA; n = 5 mice in the ctrl group and 6 mice in the TeNT group).

(J) Peri-event plots of the average speed of a mouse in the ctrl group (left) and a mouse in the TeNT group (right) across five daily classic conditioning sessions. Blue segments indicate statistically significant decrease from the baseline.

(K) Peri-event plots of the average speed for the ctrl group and the TeNT group in the fifth classic conditioning session (n = 5 mice in the ctrl group and 6 mice in the TeNT group). Blue segments indicate statistically significant decrease from the baseline. Yellow segments indicate statistically significant increase from the baseline. The highlighted regions indicate statistically differences of the average speed between two groups ($p < 0.05$; two-way ANOVA with post hoc Sidak's test).

(L) Comparison of the lowest average speed mice reached (left) and the time when mice reached the lowest average speed (right) between two groups in the fifth classic conditioning session (two-sided unpaired t test; n = 5 mice in the ctrl group and 6 mice in the TeNT group).

See Table S2 for detailed statistical tests. p values are shown in the graph. Data are means ± SEM. Scale bars, 100 μm. See also Figures S8 and S9.

photometry to monitor the neuronal activity of DRN DA neurons in the appetitive Pavlovian conditioning task (Figure 7F). Blocking the neurotransmission of DRN-projecting LPB neurons significantly reduced DRN DA neurons' responses to sucrose (Figures 7G, 7H, and S9O). Moreover, DRN DA neurons no longer acquired the learning-dependent excitatory responses to the sucrose-predicting cue (Figures 7G, 7H, and S9O). We analyzed the change in mice's locomotor behaviors during the appetitive Pavlovian conditioning task to examine whether this blockade affects conditioned behavioral responses. As the training progressed, mice in the control group gradually learned to slow down following auditory cue initiation and reached the lowest speed immediately after the onset of sucrose delivery (Figures 7J–7L). This behavioral conditioning was impaired by blocking the neurotransmission of DRN-projecting LPB neurons (Figures 7J and 7K): by the fifth conditioning section, the mice took a longer time to lower the speed. Moreover, the amount of speed change for the test mice was significantly less than the control mice (Figures 7L). These results collectively suggest that the loss of LPB inputs disrupts reward processing by DRN DA neurons.

DISCUSSION

The ability to effectively form and express memory is fundamentally important for animal behaviors. DA has been considered as a critical neuromodulator for learning and memory formation. Previous studies provide enormous insights into the circuit mechanisms of DA signaling, especially the one governed by VTA DA system, in regulating the formation of reward memory and drug addiction (Schultz et al., 1997; Hyman, 2005; Keiflin and Janak, 2015). Previous pharmacological studies that manipulated DA receptors activity in various brain areas suggest the potential involvement of DA modulation in some neuronal processes related to the expression of reward and aversive memory (Salamone et al., 1991; Ichihara et al., 1992; Nader and LeDoux, 1999; El-Ghundi et al., 2001). However, the exact role and specific DA circuits underlying the regulation of memory expression remain elusive. Here, we identified a specialized DA subsystem in the DRN that control the expression of incentive memory under normal conditions and in drug addiction. Further, we uncovered an upstream medulla input to this DRN DA subsystem that specifically regulate its reward processing and control the expression of reward memory.

In addition to supportive evidence from our anatomical mapping and fiber photometry of Ca^{2+} signals, area-specific optogenetic inhibitions in different test phases provide particularly interesting insights into distinct behavioral functions of DA neurons in the DRN and the VTA. Inhibiting DRN DA neurons blocks the expression but not the formation of both appetitive and aversive memory associated with natural stimuli and morphine administration. Using CRISPR/Cas9-mediated *in vivo* knockout, we also demonstrated that the DA transmission of DRN DA neurons is indeed critical for their behavioral functions. A previous study by Hnasko et al. reported that the DA is not required for morphine-induced CPP (Hnasko et al., 2005). The seemingly discrepancy between Hnasko et al.'s work and ours might reflect the differences between the lifelong knockout strategy used in the previous study and the acute loss-of-function strategy we used here. Compensatory mechanisms might be involved to counteract the loss of DA signaling in the transgenic DA-deficient mouse model ($Th^{-/-}$; $Dbh^{Th/+}$ mice). In fact, previous studies also reported that the activities and DA transmission of VTA DA neurons are essential for the formation of morphine-induced CPP (Chen et al., 2015; Corre et al., 2018; Yan et al., 2015). Notably, DRN DA neurons may release glutamate and neuropeptides such as vasoactive intestinal peptide (Li et al., 2016a; Matthews et al., 2016; Poulin et al., 2014, 2018), suggesting the potential engagement of multiple neurotransmitters for DRN DA neurons' behavioral functions. The DRN has abundant opioid receptors (including both mu and kappa opioid receptors) expression and binding (Mansour et al., 1995). Because of the complex subcellular localizations and signaling pathways of opioid receptors, morphine may recruit complicated local and long-range circuits that differ from natural stimuli to affect the activity of DRN DA neurons.

By contrast, inhibiting VTA DA neurons blocks the formation but not expression of morphine-associated CPP, which is consistent with the well-established role of these neurons in the formation of appetitive memory (Schultz et al., 1997; Wise, 2004; Keiflin and Janak, 2015). At both population and single-neuron level, DRN DA neurons show clear anatomical segregation from their VTA counterparts with distinct axonal projection patterns (Figure 1) and presynaptic partners (Figures 6B and S7) (Watabe-Uchida et al., 2012; Beier et al., 2015). DRN DA neurons primarily project to and form reciprocal connections with the CeA and the BNST, which are two key components in the neural circuits for regulating emotional memory. An early study indicates that DRN DA neurons mainly target areas enriched in GABAergic neurons in the CeA and the BNST (Freedman and Cassell, 1994). Therefore, this DRN DA-to-CeA/BNST circuit might constitute a parallel of the VTA-to-ventral striatum pathway and the substantia nigra pars compacta-to-dorsal striatum pathway. Both the CeA and the BNST strongly express DA receptors D1 and D2 (Scibilia et al., 1992; Kim et al., 2017). Since DRN DA neurons represent the major source of the DA drive to the CeA and the BNST, DRN DA neurons may mediate behavioral functions by cooperatively modulating neurons in these two areas. In *Drosophila*, the DA system organizes into anatomical and functional subsystems that innervate discrete compartments in the mushroom bodies (Aso et al., 2014). Among them, a DA neuron subpopulation receives neuropeptidergic input and specifically controls appetitive memory expression based on flies' energy states (Krashes et al., 2009). Therefore, segregated DA subsystems for memory formation and expression might be an evolutionally conserved principle in both vertebrates and invertebrates.

Our work substantially expands the behavioral functions of DRN DA neurons. Matthews et al. (2016) propose that DRN DA neurons encode a "loneliness" state. Our fiber photometry showed that DRN DA neurons are indeed activated following initial social encounter (Figure S2A). However, the response strength to social interaction is significantly weaker than that to food and foot shock and rapidly decreases in the following social interaction bouts (Figures S2A–S2C). The effects of manipulating DRN DA neurons on social behaviors in the previous study might reflect the contribution of these neurons to regulating the expression of incentive memory associated with social interaction. Cho et al. (2017) report

that DRN DA neurons encode salience and promote arousal. More recently, Groessl et al. (2018) show that DRN DA neurons encode aversive prediction error and gate fear learning. Here, we found that, besides responding to naturally incentive stimuli with either positive or negative valence (Figure S2) as shown in the previous studies (Cho et al., 2017; Groessl et al., 2018), DRN DA neurons can acquire excitatory responses through learning to the previously neutral cues that are conditioned with either appetitive or aversive stimuli, providing further evidence that DRN DA neurons encode incentive salience of encountered stimuli. Importantly, our experiments revealed a surprising function of these neurons in the expression of incentive memory. A wide range of neuron populations in the brain respond to salience signals and perform specific behavioral functions in addition to promoting arousal. For example, the paraventricular thalamus neurons encode multiple forms of salience and gate associative learning (Zhu et al., 2018). Neurons in the basal forebrain encode salience and guide animals' attention (Hangya et al., 2015; Lin and Nicolelis, 2008). Similarly, different subpopulations of VTA DA neurons encode either reward or aversive prediction errors and direct memory formation (de Jong et al., 2019), while manipulating VTA DA neurons' activity bidirectionally regulate arousal (Eban-Rothschild et al., 2016). Our results indicate that DRN DA neurons is dispensable for reward memory formation but controls the expression of both reward and aversive memory rather than promoting general arousal.

Using morphine as the probe to search for functionally relevant inputs to DRN DA neurons, we further identified a glutamatergic pathway from the LPB to the DRN that specifically regulates reward processing. Recent studies reveal the cell-type- and subarea-specific involvement of the LPB in sensory relay (Palmiter, 2018), food intake (De Araujo, 2009; Wu et al., 2009, 2012), salt intake (Colombari et al., 1996; Geerling and Loewy, 2007; Jarvie and Palmiter, 2017; Ryan et al., 2017), thermoregulation (Yahiro et al., 2017), and alarm signal processing (Kaur et al., 2017; Suzuki et al., 2012). Our results demonstrate that the LPB participates in reward processing and morphine-related memory expression by recruiting DRN DA neurons. DRN-projecting LPB neurons also target DRN serotonin neurons and DRN GABAergic neurons, albeit the connections are much weaker compared with DRN DA neurons (Figures S7E–S7G). Considering that central serotonin neurons are not required for morphine tolerance or morphine reward (Zhao et al., 2007), and that DRN GABAergic neurons are activated by aversive stimuli and inhibited by appetitive stimuli (Li et al., 2016b), it is likely that the observed behavioral functions of DRN-projecting LPB neurons are mainly mediated by DRN DA neurons. Intriguingly, the LPB strongly expresses the mu opioid receptor (Arvidsson et al., 1995; Chamberlin et al., 1999). Locally activating this receptor enhances Fos expression in the LPB as well as in multiple brain areas associated with reward processing (Denbleyker et al., 2009) and increases food intake (Wilson et al., 2003). Future studies will be necessary to determine the molecular mechanisms of the morphine-triggered plasticity in DRN-projecting LPB neurons. Given that the LPB-to-DRN pathway participates only in reward processing, whereas the DRN DA neurons modulate both the formation and expression of aversive memory (Figures 2F, 4D, 4E, and S3T–S3V), DRN DA neurons may engage yet-to-be identified inputs specific for aversive processing.

In summary, our study pinpoints the essential behavioral functions of the raphe DA system in controlling memory expression and unveils unique circuit mechanisms underlying opioid-associated memory expression. Further molecular profiling of DRN DA neurons and DRN-projecting LPB neurons may provide opportunities for developing future pharmacological strategies of interventions against opioid abuse.

STAR★METHODS

Detailed methods are provided in the online version of this paper and include the following:

- KEY RESOURCES TABLE
- LEAD CONTACT AND MATERIALS AVAILABILITY
- EXPERIMENTAL MODEL AND SUBJECT DETAILS
- METHOD DETAILS
  - Viral constructs and AAV packaging
  - Common surgery and virus injection
  - Single neuron reconstruction and registration
  - Behavior tests
  - Fiber photometry
  - Testing behavioral effects on Fos expression
  - Patch-clamp electrophysiology
  - Rabies screen
  - Immunohistochemistry
- QUANTIFICATION AND STATISTICAL ANALYSIS
- DATA AND CODE AVAILABILITY

SUPPLEMENTAL INFORMATION

Supplemental Information can be found online at https://doi.org/10.1016/j.neuron.2020.02.009.

ACKNOWLEDGMENTS

We thank X. Han and J. Li for their assistance with experimental reagents, K. Deisseroth (Stanford University) for the pAAV-EF1α-DIO-hChR2(H134R)-mCherry plasmid, L. Luo (Stanford University) for the pAAV-TRE-HTG plasmid, N. Shah (Stanford University) for the pAAV-FLEX-taCasp3-TEVp plasmid, T. Südhof (Stanford University) for the pAAV-DIO-GFP-2A-TeNT plasmid, N. Uchida (Harvard University) for the pAAV-DIO-TVA-mCherry plasmid, and J.H. Snyder for manuscript editing. M.L. is supported by China MOST (2015BAI08B02), NNSFC (91432114, 91632302), and the Beijing Municipal Government.

AUTHOR CONTRIBUTIONS

R.L., J.L., and M.L. designed the experiments. R.L. and J.L. performed most of the experiments. R.W. and T.Y. reconstructed single DRN DA neurons. Y. Liu performed the slice recording of GtACR1-expressing neurons. F.S. and Y. Li developed the $GRAB_{DA}$ sensor. Q.F. and Y.Z. packaged AAV viruses. A.L. and H.G. performed the fMOST imaging. R.L., J.L., and M.L. wrote the manuscript.

DECLARATION OF INTERESTS

The authors declare no competing interests.

Received: January 6, 2020
Revised: February 3, 2020
Accepted: February 10, 2020
Published: March 6, 2020

REFERENCES

Armbruster, B.N., Li, X., Pausch, M.H., Herlitze, S., and Roth, B.L. (2007). Evolving the lock to fit the key to create a family of G protein-coupled receptors potently activated by an inert ligand. Proc. Natl. Acad. Sci. USA *104*, 5163–5168.

Arvidsson, U., Riedl, M., Chakrabarti, S., Lee, J.H., Nakano, A.H., Dado, R.J., Loh, H.H., Law, P.Y., Wessendorf, M.W., and Elde, R. (1995). Distribution and targeting of a mu-opioid receptor (MOR1) in brain and spinal cord. J. Neurosci. *15*, 3328–3341.

Aso, Y., and Rubin, G.M. (2016). Dopaminergic neurons write and update memories with cell-type-specific rules. eLife *5*, e16135.

Aso, Y., Hattori, D., Yu, Y., Johnston, R.M., Iyer, N.A., Ngo, T.-T., Dionne, H., Abbott, L.F., Axel, R., Tanimoto, H., and Rubin, G.M. (2014). The neuronal architecture of the mushroom body provides a logic for associative learning. eLife *3*, e04577.

Avery, S.N., Clauss, J.A., and Blackford, J.U. (2016). The Human BNST: Functional Role in Anxiety and Addiction. Neuropsychopharmacology *41*, 126–141.

Bechara, A., Nader, K., and van der Kooy, D. (1995). Neurobiology of withdrawal motivation: evidence for two separate aversive effects produced in morphine-naive versus morphine-dependent rats by both naloxone and spontaneous withdrawal. Behav. Neurosci. *109*, 91–105.

Beier, K.T., Steinberg, E.E., DeLoach, K.E., Xie, S., Miyamichi, K., Schwarz, L., Gao, X.J., Kremer, E.J., Malenka, R.C., and Luo, L. (2015). Circuit Architecture of VTA Dopamine Neurons Revealed by Systematic Input-Output Mapping. Cell *162*, 622–634.

Beier, K.T., Kim, C.K., Hoerbelt, P., Hung, L.W., Heifets, B.D., DeLoach, K.E., Mosca, T.J., Neuner, S., Deisseroth, K., Luo, L., and Malenka, R.C. (2017). Rabies screen reveals GPe control of cocaine-triggered plasticity. Nature *549*, 345–350.

Blaiss, C.A., and Janak, P.H. (2009). The nucleus accumbens core and shell are critical for the expression, but not the consolidation, of Pavlovian conditioned approach. Behav. Brain Res. *200*, 22–32.

Buckner, R.L., Kelley, W.M., and Petersen, S.E. (1999). Frontal cortex contributes to human memory formation. Nat. Neurosci. *2*, 311–314.

Cai, Y.-Q., Wang, W., Hou, Y.-Y., Zhang, Z., Xie, J., and Pan, Z.Z. (2013). Central amygdala GluA1 facilitates associative learning of opioid reward. J. Neurosci. *33*, 1577–1588.

Chamberlin, N.L., Mansour, A., Watson, S.J., and Saper, C.B. (1999). Localization of mu-opioid receptors on amygdaloid projection neurons in the parabrachial nucleus of the rat. Brain Res. *827*, 198–204.

Chen, M., Zhao, Y., Yang, H., Luan, W., Song, J., Cui, D., Dong, Y., Lai, B., Ma, L., and Zheng, P. (2015). Morphine disinhibits glutamatergic input to VTA dopamine neurons and promotes dopamine neuron excitation. eLife *4*, e09275.

Cho, J.R., Treweek, J.B., Robinson, J.E., Xiao, C., Bremner, L.R., Greenbaum, A., and Gradinaru, V. (2017). Dorsal Raphe Dopamine Neurons Modulate Arousal and Promote Wakefulness by Salient Stimuli. Neuron *94*, 1205–1219.e8.

Cohen, J.Y., Haesler, S., Vong, L., Lowell, B.B., and Uchida, N. (2012). Neuron-type-specific signals for reward and punishment in the ventral tegmental area. Nature *482*, 85–88.

Colombari, D.S., Menani, J.V., and Johnson, A.K. (1996). Forebrain angiotensin type 1 receptors and parabrachial serotonin in the control of NaCl and water intake. Am. J. Physiol. *271*, R1470–R1476.

Corre, J., van Zessen, R., Loureiro, M., Patriarchi, T., Tian, L., Pascoli, V., and Lüscher, C. (2018). Dopamine neurons projecting to medial shell of the nucleus accumbens drive heroin reinforcement. eLife *7*, e39945.

de Araujo, I.E. (2009). Gustatory and homeostatic functions of the rodent parabrachial nucleus. Ann. N Y Acad. Sci. *1170*, 383–391.

de Jong, J.W., Afjei, S.A., Pollak Dorocic, I., Peck, J.R., Liu, C., Kim, C.K., Tian, L., Deisseroth, K., and Lammel, S. (2019). A Neural Circuit Mechanism for Encoding Aversive Stimuli in the Mesolimbic Dopamine System. Neuron *101*, 133–151.e7.

Denbleyker, M., Nicklous, D.M., Wagner, P.J., Ward, H.G., and Simansky, K.J. (2009). Activating μ-opioid receptors in the lateral parabrachial nucleus increases c-Fos expression in forebrain areas associated with caloric regulation, reward and cognition. Neuroscience *162*, 224–233.

Eban-Rothschild, A., Rothschild, G., Giardino, W.J., Jones, J.R., and de Lecea, L. (2016). VTA dopaminergic neurons regulate ethologically relevant sleep-wake behaviors. Nat. Neurosci. *19*, 1356–1366.

Ehrlich, I., Humeau, Y., Grenier, F., Ciocchi, S., Herry, C., and Lüthi, A. (2009). Amygdala inhibitory circuits and the control of fear memory. Neuron *62*, 757–771.

El-Ghundi, M., O'Dowd, B.F., and George, S.R. (2001). Prolonged fear responses in mice lacking dopamine D1 receptor. Brain Res. *892*, 86–93.

Freedman, L.J., and Cassell, M.D. (1994). Distribution of dopaminergic fibers in the central division of the extended amygdala of the rat. Brain Res. *633*, 243–252.

Geerling, J.C., and Loewy, A.D. (2007). Sodium deprivation and salt intake activate separate neuronal subpopulations in the nucleus of the solitary tract and the parabrachial complex. J. Comp. Neurol. *504*, 379–403.

Gibson, D.G., Young, L., Chuang, R.-Y., Venter, J.C., Hutchison, C.A., and Smith, H.O. (2009). Enzymatic assembly of DNA molecules up to several hundred kilobases. Nature Methods *6*, 343–345.

Gong, H., Xu, D., Yuan, J., Li, X., Guo, C., Peng, J., Li, Y., Schwarz, L.A., Li, A., Hu, B., et al. (2016). High-throughput dual-colour precision imaging for brain-wide connectome with cytoarchitectonic landmarks at the cellular level. Nat. Commun. *7*, 12142.

Govorunova, E.G., Sineshchekov, O.A., Janz, R., Liu, X., and Spudich, J.L. (2015). NEUROSCIENCE. Natural light-gated anion channels: A family of microbial rhodopsins for advanced optogenetics. Science *349*, 647–650.

Groessl, F., Munsch, T., Meis, S., Griessner, J., Kaczanowska, J., Pliota, P., Kargl, D., Badurek, S., Kraitsy, K., Rassoulpour, A., et al. (2018). Dorsal tegmental dopamine neurons gate associative learning of fear. Nat. Neurosci. *21*, 952–962.

Gunaydin, L.A., Grosenick, L., Finkelstein, J.C., Kauvar, I.V., Fenno, L.E., Adhikari, A., Lammel, S., Mirzabekov, J.J., Airan, R.D., Zalocusky, K.A., et al. (2014). Natural Neural Projection Dynamics Underlying Social Behavior. Cell *157*, 1535–1551.

Hangya, B., Ranade, S.P., Lorenc, M., and Kepecs, A. (2015). Central Cholinergic Neurons Are Rapidly Recruited by Reinforcement Feedback. Cell *162*, 1155–1168.

Harris, G.C., Wimmer, M., Byrne, R., and Aston-Jones, G. (2004). Glutamate-associated plasticity in the ventral tegmental area is necessary for conditioning environmental stimuli with morphine. Neuroscience *129*, 841–847.

Hasue, R.H., and Shammah-Lagnado, S.J. (2002). Origin of the dopaminergic innervation of the central extended amygdala and accumbens shell: a combined retrograde tracing and immunohistochemical study in the rat. J. Comp. Neurol. *454*, 15–33.

Hnasko, T.S., Sotak, B.N., and Palmiter, R.D. (2005). Morphine reward in dopamine-deficient mice. Nature *438*, 854–857.

Hokfelt, T. (1984). Distribution maps of tyrosinehydroxylase-immunoreactive neurons in the rat brain. Handb. Chem. Neuroanat. Class. Transm. CNS *2*, 277–379.

Hyman, S.E. (2005). Addiction: a disease of learning and memory. Am. J. Psychiatry *162*, 1414–1422.

Hyman, S.E., Malenka, R.C., and Nestler, E.J. (2006). Neural mechanisms of addiction: the role of reward-related learning and memory. Annu. Rev. Neurosci. *29*, 565–598.

Ichihara, K., Nabeshima, T., and Kameyama, T. (1992). Effects of dopamine receptor agonists on passive avoidance learning in mice: interaction of dopamine D1 and D2 receptors. Eur. J. Pharmacol. *213*, 243–249.

Ikemoto, S. (2007). Dopamine reward circuitry: two projection systems from the ventral midbrain to the nucleus accumbens-olfactory tubercle complex. Brain Res. Brain Res. Rev. *56*, 27–78.

Jarvie, B.C., and Palmiter, R.D. (2017). HSD2 neurons in the hindbrain drive sodium appetite. Nat. Neurosci. *20*, 167–169.

Johnson, S.W., and North, R.A. (1992). Opioids excite dopamine neurons by hyperpolarization of local interneurons. J. Neurosci. *12*, 483–488.

Kaun, K.R., and Rothenfluh, A. (2017). Dopaminergic rules of engagement for memory in Drosophila. Curr. Opin. Neurobiol. *43*, 56–62.

Kaur, S., Wang, J.L., Ferrari, L., Thankachan, S., Kroeger, D., Venner, A., Lazarus, M., Wellman, A., Arrigoni, E., Fuller, P.M., and Saper, C.B. (2017). A Genetically Defined Circuit for Arousal from Sleep during Hypercapnia. Neuron *96*, 1153–1167.e5.

Keiflin, R., and Janak, P.H. (2015). Dopamine Prediction Errors in Reward Learning and Addiction: From Theory to Neural Circuitry. Neuron *88*, 247–263.

Kim, J., Zhang, X., Muralidhar, S., LeBlanc, S.A., and Tonegawa, S. (2017). Basolateral to Central Amygdala Neural Circuits for Appetitive Behaviors. Neuron *93*, 1464–1479.e5.

Krashes, M.J., DasGupta, S., Vreede, A., White, B., Armstrong, J.D., and Waddell, S. (2009). A neural circuit mechanism integrating motivational state with memory expression in Drosophila. Cell *139*, 416–427.

Li, B. (2019). Central amygdala cells for learning and expressing aversive emotional memories. Curr. Opin. Behav. Sci. *26*, 40–45.

Li, Y.Q., Xue, Y.X., He, Y.Y., Li, F.Q., Xue, L.F., Xu, C.M., Sacktor, T.C., Shaham, Y., and Lu, L. (2011). Inhibition of PKMzeta in nucleus accumbens core abolishes long-term drug reward memory. J. Neurosci. *31*, 5436–5446.

Li, Y., Dong, X., Li, S., and Kirouac, G.J. (2014). Lesions of the posterior paraventricular nucleus of the thalamus attenuate fear expression. Front. Behav. Neurosci. *8*, 94.

Li, Y., Gong, H., Yang, X., Yuan, J., Jiang, T., Li, X., Sun, Q., Zhu, D., Wang, Z., Luo, Q., et al. (2017). TDat: An Efficient Platform for Processing Petabyte-Scale Whole-Brain Volumetric Images. Front Neural Circuits *11*, https://doi.org/10.3389/fncir.2017.00051.

Li, C., Sugam, J.A., Lowery-Gionta, E.G., McElligott, Z.A., McCall, N.M., Lopez, A.J., McKlveen, J.M., Pleil, K.E., and Kash, T.L. (2016a). Mu Opioid Receptor Modulation of Dopamine Neurons in the Periaqueductal Gray/Dorsal Raphe: A Role in Regulation of Pain. Neuropsychopharmacology *41*, 2122–2132.

Li, Y., Zeng, J., Zhang, J., Yue, C., Zhong, W., Liu, Z., Feng, Q., and Luo, M. (2018). Hypothalamic Circuits for Predation and Evasion. Neuron *97*, 911–924.e5.

Li, Y., Zhong, W., Wang, D., Feng, Q., Liu, Z., Zhou, J., Jia, C., Hu, F., Zeng, J., Guo, Q., et al. (2016b). Serotonin neurons in the dorsal raphe nucleus encode reward signals. Nat. Commun. *7*, 10503.

Lin, S.-C., and Nicolelis, M.A.L. (2008). Neuronal ensemble bursting in the basal forebrain encodes salience irrespective of valence. Neuron *59*, 138–149.

Lin, R., Wang, R., Yuan, J., Feng, Q., Zhou, Y., Zeng, S., Ren, M., Jiang, S., Ni, H., Zhou, C., et al. (2018). Cell-type-specific and projection-specific brain-wide reconstruction of single neurons. Nat. Methods *15*, 1033–1036.

Lisman, J.E., and Grace, A.A. (2005). The hippocampal-VTA loop: controlling the entry of information into long-term memory. Neuron *46*, 703–713.

Lüscher, C. (2016). The Emergence of a Circuit Model for Addiction. Annu. Rev. Neurosci. *39*, 257–276.

Mansour, A., Fox, C.A., Akil, H., and Watson, S.J. (1995). Opioid-receptor mRNA expression in the rat CNS: anatomical and functional implications. Trends Neurosci. *18*, 22–29.

Matthews, G.A., Nieh, E.H., Vander Weele, C.M., Halbert, S.A., Pradhan, R.V., Yosafat, A.S., Glober, G.F., Izadmehr, E.M., Thomas, R.E., Lacy, G.D., et al. (2016). Dorsal Raphe Dopamine Neurons Represent the Experience of Social Isolation. Cell *164*, 617–631.

McGaugh, J.L., Cahill, L., and Roozendaal, B. (1996). Involvement of the amygdala in memory storage: interaction with other brain systems. Proc. Natl. Acad. Sci. USA *93*, 13508–13514.

Miyamichi, K., Amat, F., Moussavi, F., Wang, C., Wickersham, I., Wall, N.R., Taniguchi, H., Tasic, B., Huang, Z.J., He, Z., et al. (2011). Cortical representations of olfactory input by trans-synaptic tracing. Nature *472*, 191–196.

Nader, K., and LeDoux, J. (1999). The dopaminergic modulation of fear: quinpirole impairs the recall of emotional memories in rats. Behav. Neurosci. *113*, 152–165.

Nestler, E.J. (2001). Neurobiology. Total recall-the memory of addiction. Science *292*, 2266–2267.

Ni, H., Tran, C., Feng, Z., Chen, S., Zhang, Z., Li, W., Guan, Y., Gong, H., Luo, Q., and Li, A. (2020). A robust image registration interface for large volume brain atlas. Sci. Rep. *10*, 2139.

Packard, M.G., and Knowlton, B.J. (2002). Learning and memory functions of the Basal Ganglia. Annu. Rev. Neurosci. *25*, 563–593.

Palmiter, R.D. (2018). The Parabrachial Nucleus: CGRP Neurons Function as a General Alarm. Trends Neurosci. *41*, 280–293.

Poulin, J.-F., Zou, J., Drouin-Ouellet, J., Kim, K.-Y.A., Cicchetti, F., and Awatramani, R.B. (2014). Defining midbrain dopaminergic neuron diversity by single-cell gene expression profiling. Cell Rep. *9*, 930–943.

Poulin, J.-F., Caronia, G., Hofer, C., Cui, Q., Helm, B., Ramakrishnan, C., Chan, C.S., Dombeck, D.A., Deisseroth, K., and Awatramani, R. (2018). Mapping projections of molecularly defined dopamine neuron subtypes using intersectional genetic approaches. Nat. Neurosci. *21*, 1260–1271.

Preston, A.R., and Eichenbaum, H. (2013). Interplay of hippocampus and prefrontal cortex in memory. Curr. Biol. *23*, R764–R773.

Ran, F.A., Cong, L., Yan, W.X., Scott, D.A., Gootenberg, J.S., Kriz, A.J., Zetsche, B., Shalem, O., Wu, X., Makarova, K.S., et al. (2015). *In vivo* genome editing using *Staphylococcus aureus* Cas9. Nature *520*, 186–191.

Robinson, T.E., and Kolb, B. (1997). Persistent structural modifications in nucleus accumbens and prefrontal cortex neurons produced by previous experience with amphetamine. J. Neurosci. *17*, 8491–8497.

Ryan, P.J., Ross, S.I., Campos, C.A., Derkach, V.A., and Palmiter, R.D. (2017). Oxytocin-receptor-expressing neurons in the parabrachial nucleus regulate fluid intake. Nat. Neurosci. *20*, 1722–1733.

Salamone, J.D., Steinpreis, R.E., McCullough, L.D., Smith, P., Grebel, D., and Mahan, K. (1991). Haloperidol and nucleus accumbens dopamine depletion suppress lever pressing for food but increase free food consumption in a novel food choice procedure. Psychopharmacology (Berl.) *104*, 515–521.

Schultz, W., Dayan, P., and Montague, P.R. (1997). A neural substrate of prediction and reward. Science *275*, 1593–1599.

Scibilia, R.J., Lachowicz, J.E., and Kilts, C.D. (1992). Topographic nonoverlapping distribution of D1 and D2 dopamine receptors in the amygdaloid nuclear complex of the rat brain. Synapse *11*, 146–154.

Scoville, W.B., and Milner, B. (1957). Loss of recent memory after bilateral hippocampal lesions. J. Neurol. Neurosurg. Psychiatry *20*, 11–21.

Shang, C., Chen, Z., Liu, A., Li, Y., Zhang, J., Qu, B., Yan, F., Zhang, Y., Liu, W., Liu, Z., et al. (2018). Divergent midbrain circuits orchestrate escape and freezing responses to looming stimuli in mice. Nat. Commun. *9*, 1232.

Soria-Gómez, E., Busquets-Garcia, A., Hu, F., Mehidi, A., Cannich, A., Roux, L., Louit, I., Alonso, L., Wiesner, T., Georges, F., et al. (2015). Habenular CB1 Receptors Control the Expression of Aversive Memories. Neuron *88*, 306–313.

Squire, L.R. (1986). Mechanisms of memory. Science *232*, 1612–1619.

Stamatakis, A.M., Sparta, D.R., Jennings, J.H., McElligott, Z.A., Decot, H., and Stuber, G.D. (2014). Amygdala and bed nucleus of the stria terminalis circuitry: Implications for addiction-related behaviors. Neuropharmacology *76, Part B*, 320–328.

Sun, F., Zeng, J., Jing, M., Zhou, J., Feng, J., Owen, S.F., Luo, Y., Li, F., Wang, H., Yamaguchi, T., et al. (2018). A Genetically Encoded Fluorescent Sensor

Enables Rapid and Specific Detection of Dopamine in Flies, Fish, and Mice. Cell *174*, 481–496.e19.

Suzuki, T., Sugiyama, Y., and Yates, B.J. (2012). Integrative responses of neurons in parabrachial nuclei to a nauseogenic gastrointestinal stimulus and vestibular stimulation in vertical planes. Am. J. Physiol. Regul. Integr. Comp. Physiol. *302*, R965–R975.

Tervo, D.G.R., Hwang, B.-Y., Viswanathan, S., Gaj, T., Lavzin, M., Ritola, K.D., Lindo, S., Michael, S., Kuleshova, E., Ojala, D., et al. (2016). A Designer AAV Variant Permits Efficient Retrograde Access to Projection Neurons. Neuron *92*, 372–382.

Tiklová, K., Björklund, Å.K., Lahti, L., Fiorenzano, A., Nolbrant, S., Gillberg, L., Volakakis, N., Yokota, C., Hilscher, M.M., Hauling, T., et al. (2019). Single-cell RNA sequencing reveals midbrain dopamine neuron diversity emerging during mouse brain development. Nat. Commun. *10*, 581.

Ungless, M.A., Whistler, J.L., Malenka, R.C., and Bonci, A. (2001). Single cocaine exposure *in vivo* induces long-term potentiation in dopamine neurons. Nature *411*, 583–587.

Vranjkovic, O., Pina, M., Kash, T.L., and Winder, D.G. (2017). The bed nucleus of the stria terminalis in drug-associated behavior and affect: A circuit-based perspective. Neuropharmacology *122*, 100–106.

Watabe-Uchida, M., Zhu, L., Ogawa, S.K., Vamanrao, A., and Uchida, N. (2012). Whole-brain mapping of direct inputs to midbrain dopamine neurons. Neuron *74*, 858–873.

Wei, C., Han, X., Weng, D., Feng, Q., Qi, X., Li, J., and Luo, M. (2018). Response dynamics of midbrain dopamine neurons and serotonin neurons to heroin, nicotine, cocaine, and MDMA. Cell Discov. *4*, 60.

Wilson, J.D., Nicklous, D.M., Aloyo, V.J., and Simansky, K.J. (2003). An orexigenic role for μ-opioid receptors in the lateral parabrachial nucleus. Am. J. Physiol. Regul. Integr. Comp. Physiol. *285*, R1055–R1065.

Wise, R.A. (2004). Dopamine, learning and motivation. Nat. Rev. Neurosci. *5*, 483–494.

Wise, R.A., and Koob, G.F. (2014). The development and maintenance of drug addiction. Neuropsychopharmacology *39*, 254–262.

Wu, Q., Boyle, M.P., and Palmiter, R.D. (2009). Loss of GABAergic signaling by AgRP neurons to the parabrachial nucleus leads to starvation. Cell *137*, 1225–1234.

Wu, Q., Clark, M.S., and Palmiter, R.D. (2012). Deciphering a neuronal circuit that mediates appetite. Nature *483*, 594–597.

Yahiro, T., Kataoka, N., Nakamura, Y., and Nakamura, K. (2017). The lateral parabrachial nucleus, but not the thalamus, mediates thermosensory pathways for behavioural thermoregulation. Sci. Rep. *7*, 5031.

Yan, T., Rizak, J.D., Wang, J., Yang, S., Ma, Y., and Hu, X. (2015). Severe dopaminergic neuron loss in rhesus monkey brain impairs morphine-induced conditioned place preference. Front. Behav. Neurosci. *9*, 273.

Yang, C.F., Chiang, M.C., Gray, D.C., Prabhakaran, M., Alvarado, M., Juntti, S.A., Unger, E.K., Wells, J.A., and Shah, N.M. (2013). Sexually dimorphic neurons in the ventromedial hypothalamus govern mating in both sexes and aggression in males. Cell *153*, 896–909.

Zarrindast, M.-R., Rezayof, A., Sahraei, H., Haeri-Rohani, A., and Rassouli, Y. (2003). Involvement of dopamine D1 receptors of the central amygdala on the acquisition and expression of morphine-induced place preference in rat. Brain Res. *965*, 212–221.

Zhang, J., Tan, L., Ren, Y., Liang, J., Lin, R., Feng, Q., Zhou, J., Hu, F., Ren, J., Wei, C., et al. (2016). Presynaptic Excitation via GABAB Receptors in Habenula Cholinergic Neurons Regulates Fear Memory Expression. Cell *166*, 716–728.

Zhao, Z.-Q., Gao, Y.-J., Sun, Y.-G., Zhao, C.-S., Gereau, R.W., 4th, and Chen, Z.-F. (2007). Central serotonergic neurons are differentially required for opioid analgesia but not for morphine tolerance or morphine reward. Proc. Natl. Acad. Sci. USA *104*, 14519–14524.

Zhong, W., Li, Y., Feng, Q., and Luo, M. (2017). Learning and Stress Shape the Reward Response Patterns of Serotonin Neurons. J. Neurosci. *37*, 8863–8875.

Zhu, Y., Wienecke, C.F.R., Nachtrab, G., and Chen, X. (2016). A thalamic input to the nucleus accumbens mediates opiate dependence. Nature *530*, 219–222.

Zhu, Y., Nachtrab, G., Keyes, P.C., Allen, W.E., Luo, L., and Chen, X. (2018). Dynamic salience processing in paraventricular thalamus gates associative learning. Science *362*, 423–429.

Zimmerman, J.M., Rabinak, C.A., McLachlan, I.G., and Maren, S. (2007). The central nucleus of the amygdala is essential for acquiring and expressing conditional fear after overtraining. Learn. Mem. *14*, 634–644.

STAR★METHODS

KEY RESOURCES TABLE

REAGENT or RESOURCE	SOURCE	IDENTIFIER
Antibodies		
Rabbit polyclonal anti-TH	Millipore	Cat# AB152; RRID:AB_390204
Chicken polyclonal anti-TH	Abcam	Cat# ab76442; RRID:AB_1524535
Rabbit monoclonal anti-c-Fos	Cell Signaling Technology	Cat# 2250; RRID:AB_2247211
Rabbit polyclonal anti-GFP	Thermo Fisher Scientific	Cat# A10259; RRID:AB_2534021
Rat monoclonal anti-HA	Roche	Cat# 11815016001; RRID:AB_390914
Goat Anti-Rabbit IgG (H+L) Cy3	Jackson ImmunoResearch Labs	Cat# 111-165-144; RRID:AB_2338006
Donkey Anti-Chicken IgY (IgG) (H+L) Alexa Fluor 488	Jackson ImmunoResearch Labs	Cat# 703-545-155; RRID:AB_2340375
Goat Anti-Rat IgG (H+L) Cy3	Thermo Fisher Scientific	Cat# A10522; RRID:AB_2534031
Bacterial and Virus Strains		
AAV2-CAG-DIO-GtACR1-P2A-GFP	Minmin Luo lab (Li et al., 2018)	N/A
AAV2-EF1a-DIO-mCherry	Minmin Luo lab (this paper)	N/A
AAV2-EF1a-DIO-mGFP	Minmin Luo lab (Li et al., 2018)	N/A
AAV2-EF1a-DIO-GCaMP6m	Minmin Luo lab (Li et al., 2018)	N/A
AAV2-EF1a-DIO-ChR2-mCherry	Minmin Luo lab (Li et al., 2018)	N/A
AAV2-TRE-DIO-FLPo	Minmin Luo lab (Lin et al., 2018)	N/A
AAV2-TRE-fDIO-GFP-IRES-tTA	Minmin Luo lab (Lin et al., 2018)	N/A
AAV2-EF1a-DIO-H2B-GFP	Minmin Luo lab (Lin et al., 2018)	N/A
AAV2-EF1a-FLEX-taCasp3-TEVp	Minmin Luo lab (Zhang et al., 2016)	N/A
AAV2-DIO-GFP-2A-TeNT	Minmin Luo lab (this paper)	N/A
AAV2-EF1a-fDIO-mScarlet-2A-TeNT	Minmin Luo lab (this paper)	N/A
AAV2-EF1a-fDIO-mScarlet	Minmin Luo lab (this paper)	N/A
AAV2-EF1a-fDIO-H2B-mCherry	Minmin Luo lab (this paper)	N/A
AAV2-EF1a-DIO-TVA-mCherry	Minmin Luo lab (this paper)	N/A
AAV2-CMV-SaCas9-U6-sgRNA-GFP	Minmin Luo lab (this paper)	N/A
AAV2-CMV-SaCas9-U6-sgRNA-TH	Minmin Luo lab (this paper)	N/A
AAV2-hSyn-GRAB$_{DA2m}$	Minmin Luo lab (this paper)	N/A
rAAV2-retro-hSyn-Cre (AAVretro-Cre)	Shanghai Taitool Bioscience	AAV2/2Retro-S0278
rAAV2-retro-hSyn-FLPo (AAVretro-FLPo)	Shanghai Taitool Bioscience	AAV2/2Retro-S0271
AAV2-hEF1a-fDIO-hM4D(Gi)-mCherry-WPRE-pA	Shanghai Taitool Bioscience	AAV2/9-S0336-9-H20
AAV2-hEF1a-fDIO-hChR2(H134R)-mCherry-WPRE-pA	Shanghai Taitool Bioscience	AAV2/9-S0404
AAV2-EF1a-DIO-RVG-WPRE-pA	BrainVTA Co., China	PT-0023
RG-deleted EGFP-expressing EnvA-rabies (RV*dG*-GFP)	BrainVTA Co., China	R01001
Chemicals, Peptides, and Recombinant Proteins		
Tetrodotoxin (TTX)	Tocris	Cat# 1078
4-Aminopyridine (4-AP)	Tocris	Cat# 0940
6, 7-dinitroquinoxaline-2, 3-dione (DNQX)	Sigma-Aldrich	Cat# D0540
Clozapine N-oxide	Hello Bio.	HB6149

(*Continued on next page*)

Continued

REAGENT or RESOURCE	SOURCE	IDENTIFIER
Experimental Models: Organisms/Strains		
Mouse: DAT-Cre	The Jackson Laboratory	006660
Mouse: Vgat-Cre	The Jackson Laboratory	028862
Mouse: Sert-Cre	UC Davis	031028-UCD
Mouse: C57BL/6N	Beijing Vital River Laboratory Animal Technology Co., Ltd. (China)	N/A
Oligonucleotides		
sgRNA-*TH*: 5′- TTTCAAAGCCCGAGACA GTGAG	Thermo Fisher Scientific	N/A
sgRNA-*GFP*: 5′-GGCAACATCCTGGGGC ACAAGC	Thermo Fisher Scientific	N/A
Recombinant DNA		
pAAV-TRE-HTG	Gift of Dr. Liqun Luo (Miyamichi et al., 2011)	N/A
pAAV-EF1a-DIO-hChR2(H134R)-mCherry	Gift of Dr. Karl Deisseroth	Addgene #20297; RRID: Addgene_20297
pAAV-FLEX-taCasp3-TEVp	Gift of Dr. Nirao Shah (Yang et al., 2013)	Addgene #45580; RRID: Addgene_45580
pAAV-DIO-GFP-2A-TeNT	Gift of Dr. Thomas Südhof (Shang et al., 2018)	N/A
pAAV-DIO-TVA-mCherry	Gift of Dr. Naoshige Uchida (Watabe-Uchida et al., 2012)	Addgene #38044; RRID: Addgene_38044
pX601	Gift of Dr. Feng Zhang (Ran et al., 2015)	Addgene #61591; RRID: Addgene_61591
pAAV-hSyn-GRAB$_{DA2m}$	Gift of Dr. Yulong Li (unpublished data)	N/A
Software and Algorithms		
MATLAB	MathWorks	R2014b
GraphPad Prism 6	GraphPad	https://www.graphpad.com/
Labview 2015	National Instruments	https://www.ni.com/en-us.html
OlyVIA 2.7	Olympus	https://olyvia.software.informer.com/
(Fiji is just) ImageJ 2.0.0	NIH	https://imagej.nih.gov/ij/
Amira 5.4.1 with TDatplug-in	Thermo Fisher Scientific; Li et al., 2017	https://www.thermofisher.com/us/en/home/industrial/electron-microscopy/electron-microscopy-instruments-workflow-solutions/3d-visualization-analysis-software/amira-life-sciences-biomedical.html
R 3.5.3	R Core Team	https://www.r-project.org/
Other		
Fiber photometry system	Set up by Nanjing ThinkerTech	N/A
Optical fiber	Thorlabs	FT200UMT
Ceramic ferrule	Fiblaser Technology	N/A
Cannula	RWD (China)	62004

LEAD CONTACT AND MATERIALS AVAILABILITY

Further information and requests for resources and programs should be directed to and will be fulfilled by the Lead Contact, Minmin Luo (luominmin@nibs.ac.cn). All unique reagents generated in this study are available from the Lead Contact with a completed Materials Transfer Agreement.

EXPERIMENTAL MODEL AND SUBJECT DETAILS

Animal care and use strictly followed the approval of the Animal Care and Use Committee of the National Institute of Biological Sciences, Beijing (Approval ID: NIBS2018M0049) in accordance with the Regulations for the Administration of Affairs Concerning Experimental Animals of China. DAT-Cre mice (JAX Strain 006660) and Vgat-Cre mice (JAX Strain 028862) were obtained from the Jackson

Laboratory. Sert-Cre mice (031028-UCD) were obtained from the University of California, Davis. C57BL/6N mice were purchased from Beijing Vital River Laboratory Animal Technology Co., Ltd (China). Adult (8-12 weeks old) DAT-Cre, Vgat-Cre and Sert-Cre mice of either sex and male C57BL/6N mice were used. Mice were maintained with a 12/12 hour photoperiod (light on at 8AM) and were provided food and water *ad libitum*, except for the food-restricted mice in the high-fat food (HFF)-induced conditioned place preference (CPP) test and the food preference test, the food-deprived mice for HFF fiber photometry, and the water-deprived mice for sucrose intake fiber photometry.

METHOD DETAILS

Viral constructs and AAV packaging

AAV vectors carrying DIO-GtACR1-P2A-GFP, DIO-mCherry, DIO-ChR2-mCherry, DIO-mGFP, DIO-GCaMP6m, TRE-DIO-FLPo, or TRE-fDIO-GFP-IRES-tTA were constructed as previously described (Li et al., 2018; Lin et al., 2018). To construct the pAAV-DIO-H2B-GFP vector, the *H2B-GFP* sequence was amplified by PCR (AP221, Transgen Biotech) from pAAV-TRE-HTG (Miyamichi et al., 2011). *H2B-GFP* was then inserted into the DIO cassette of pAAV-EF1a-DIO-hChR2(H134R)-mCherry (simplified as pAAV-DIO-ChR2-mCherry, Addgene #20297, kindly provided by Dr. Karl Deisseroth at Stanford University) by replacing the original *hChR2(H134R)-mCherry* sequence. The pAAV-FLEX-taCasp3-TEVp plasmid (Addgene #45580) was kindly provided by Dr. Nirao Shah (Stanford University). The pAAV-DIO-GFP-2A-TeNT plasmid was kindly provided by Dr. Thomas Südhof (Stanford University) (Shang et al., 2018). To construct the pAAV-fDIO-mScarlet-2A-TeNT plasmid, The *mScarlet* and *2A-TeNT* sequences were amplified by PCR and cloned in to the pAAV-TRE-fDIO backbone using Gibson assembly (Gibson et al., 2009; Lin et al., 2018). The fDIO-mScarlet-2A-TeNT cassette was then subcloned into the pAAV-DIO-ChR2-mCherry plasmid by replacing the original DIO cassette. To construct the pAAV-fDIO-mScarlet and pAAV-fDIO-H2B-mCherry, the *mScarlet*, *H2B*, and mCherry sequences were respectively amplified by PCR and cloned into the pAAV-fDIO backbone using Gibson assembly. The pAAV-DIO-TVA-mCherry plasmid (Addgene #38044) was kindly provided by Dr. Naoshige Uchida (Harvard University). The pAAV-hSyn-GRAB$_{DA2m}$ plasmid was kindly provided by Dr. Yulong Li (Peking University). The pX601 plasmid (Addgene #61591) was kindly provided by Dr. Feng Zhang (MIT). The sgRNAs targeting *tyrosine hydroxylase* (*TH*, 5′- TTTCAAAGCCCGAGACAGTGAG) or *GFP* (5′-GGCAACATCCTGGGGCACAAGC) was designed using the web tool Benchling (https://benchling.com/crispr), and subsequently synthesized and cloned into the original pX601 plasmids following the SaCas9 user manual (Ran et al., 2015).

AAV vectors were packaged into the AAV2/9 serotype with titers of 1-5 × 10^{12} viral genomes (v.g.)/mL as previously described (Li et al., 2018). rAAV2-retro-hSyn-Cre (simplified as AAVretro-Cre, 10^{13} v.g./mL), rAAV2-retro-hSyn-FLPo (simplified as AAVretro-FLPo, 10^{13} v.g./mL), AAV2-hEF1a-fDIO-hM4D(Gi)-mCherry-WPRE-pA (10^{12} v.g./mL) and AAV-hEF1a-fDIO-hChR2(H134R)-mCherry-WPRE-pA (10^{12} v.g./mL) were purchased from Shanghai Taitool Bioscience Co., China. AAV2-EF1a-DIO-RVG-WPRE-pA (10^{12} v.g./mL) and G-deleted EnvA-rabies (simplified as RV*dG*-GFP, 10^{8} infecting units/mL) were purchased from BrainVTA Co., China.

Common surgery and virus injection

Mice were anaesthetized with pentobarbital (i.p., 80 mg/kg) before surgery, and then placed in a mouse stereotaxic instrument. After disinfection with 0.3% hydrogen peroxide, a small incision of the scalp was created to expose the skull. Then, 0.3% hydrogen peroxide was applied to clean the skull, and craniotomy was conducted. The following coordinates were used to target specific brain areas: 5.0 mm posterior to the bregma and 2.5 mm ventral to the skull surface with a 15° angle (posterior to anterior) for the dorsal raphe (DRN); 5.2 mm posterior to the bregma, 1.5 mm lateral to midline, and 3.35 mm ventral to the skull surface for the lateral parabrachial nucleus (LPB); 3.2 mm posterior to the bregma, 1.68 mm lateral to midline, and 4.56 mm ventral to the skull surface with a 15° angle (lateral to middle) for the ventral tegmental area (VTA); 1.3 mm posterior to the bregma, 2.6 mm lateral to midline, and 3.7 mm ventral to the skull surface for the central amygdala (CeA); 0.26 mm posterior to the bregma, 0.875 mm lateral to midline, and 3.6 mm ventral to the skull surface for the bed nucleus of the stria terminalis (BNST).

Injections were performed using a microsyringe pump (Nanoliter 2010 Injector, WPI). A Micro controller (WPI) was used to deliver the virus solution to the target areas at a rate of 23 or 46 nL/min. Detailed virus injection paradigms are provided in Table S1.

For optogenetic stimulation and fiber photometry experiments, optical fiber implantation was carried out immediately after virus injection. A piece of optical fiber (FT200UMT, Thorlabs) was fit into an LC-sized ceramic fiber ferrule (230 mm O.D., 0.37 NA; Shanghai Fiblaser, China). The optical fiber was implanted over the target brain areas with the tip 0.1 mm above the virus injection sites. The ceramic ferrule was supported with a skull-penetrating M1 screw and dental acrylic. For intracranial Clozapine-N-oxide (CNO) injection, a cannula (62004, RWD Co., China) was implanted over the DRN one week after AAV injection. For sucrose delivery during fiber photometry, the intraoral cheek fistula was implanted one week after AAV injection using a previously-described procedure (Zhong et al., 2017). After the implantation of intraoral cheek fistula, mice were housed individually to prevent potential damage to the tubes. All subsequent experiments were performed at least 2 weeks after virus injection to allow sufficient time for transgene expression and animal recovery.

Single neuron reconstruction and registration

Protocols for single neuron reconstruction and registration were based on previously published methods with minor modifications (Lin et al., 2018). Briefly, mice were sacrificed and perfused 3 weeks after virus injection. Fluorescent micro-optical sectioning

tomography (fMOST) imaging was performed using previously published methods (Gong et al., 2016). Data were reformatted by the TDat platform (Li et al., 2017). The structures of labeled neurons were annotated by manual skeletonization in the Amira Software (Thermo Fisher Scientific). Subsequently, neuron reconstructions from different datasets were registered to the Allen Institute common coordinate framework version 3 (CCFv3) using BrainsMapi (Ni et al., 2020). Fiber length quantifications were performed with custom MATLAB codes.

Behavior tests

HFF-induced CPP test

Place preference training was performed in a custom-made three-compartment CPP apparatus. The CPP apparatus comprised two side chambers (26 × 23 × 26, L × W × H in cm), each with distinct patterns on its floors and walls: one side chamber had a stainless-steel grid floor and was striped vertically with alternating 2-cm black and white tape bands on the wall; the other side chamber had a stainless-steel mesh floor and was striped horizontally with alternating 2-cm yellow and gray tape bands. These two side chambers were separated by a neutral area lacking any decoration (11.5 × 23 × 26, L × W × H cm) that had opaque plastic walls and smooth metal floors.

Food intake was adjusted to maintain mice at ~85% of their initial *ad libitum*-fed body weight. During the HFF-induced CPP test, normal chow was provided 18 h before subsequent behavioral assays. For acclimatization, a small amount of HFF chow was given to mice in their home cages on the day before the pretest. On day 1 (the pretest phase), mice were allowed to freely explore the CPP apparatus for 30 min to assess their baseline place preferences. Any mouse that exhibited a strong initial preference for one of the side chambers (greater than 4.5-min difference) was pretested again until the strong initial preference was reduced. On days 2-9 (the conditioning phase), mice were confined to one side compartment for 15 min. The initially less preferred side was paired with a Petri dish containing HFF chow. The initially preferred side of the chamber was paired with an empty Petri dish. The Petri dish was placed under the floor and was inaccessible to the mice. The sessions with the HFF or empty Petri dishes were alternated on successive days. On day 10 (the test phase), mice were again allowed to freely explore the CPP apparatus for 30 min, as on day 1.

For optogenetic inhibition in the conditioning phase, blue laser pulses (473 nm; 3-5 mW at the fiber tip; 5 s on, 5 s off) were delivered during HFF sessions. For optogenetic inhibition in the test phase, constant blue laser light (473 nm; 3-5 mW at the fiber tip) was delivered when mice were in the HFF-paired chamber. To minimize heat-related tissue damage, the laser was turned off temporarily (for 15 s) if it had been on continuously for 30 s.

All behaviors were recorded at 20 frames per second with a camera above the apparatus. The locations of the mouse were tracked from the video recording data using a custom MATLAB program. The CPP score was calculated by subtracting the ratio of time spent in empty Petri dish-paired chamber from the ratio of time spent in HFF-paired chamber. The ΔCPP score was calculated as the difference between the initial CPP score in the pretest and the CPP score in the test phase.

Food preference test

The food preference test was conducted using an illuminated test chamber (40 × 30 × 30, L × W × H in cm) one day after the HFF-induced CPP test. Mice were food-restricted to maintain at ~85% of their initial *ad libitum*-fed body weight. Before starting tests, two Petri dishes containing either HFF or normal chow powders (CF) were placed in the diagonal corners of the test chamber (Figure S3C). Mice were placed individually in the test chamber, where they had access to both types of food, and were allowed to freely explore the chamber for 15 min. All behaviors were recorded with a camera above the apparatus and analyzed using a custom MATLAB program. The HFF preference was calculated as the ratio of high fat food consumed to the total food consumed (measured as mass in g).

Real-time place aversion test

The real-time place aversion test was conducted using a custom-made two-compartment CPP apparatus. One side chamber was decorated with horizontal black stripes, and another side chamber was decorated with vertical black stripes. A white filter paper was used as the floor for both chambers. The stimulation chamber for each mouse was assigned in a counterbalanced way. Two conditioning sessions were applied in two consecutive days. Each session lasted for 20 min. For optogenetic inhibition of both DRN and VTA dopamine (DA) neurons, a constant blue laser (473 nm; 3-5 mW at the fiber tip) was delivered when mice were in the stimulation chamber. To minimize potential tissue damage, the laser was temporarily turned off for 15 s if it had been on continuously for 30 s. For optogenetic activation of DRN DA neurons, a blue laser (473 nm; one train of 8 pulses per second, 5 ms pulse width, 30Hz; according to Matthews et al., 2016) was delivered when mice were in the stimulation chamber.

Fear conditioning and extinction test

The detailed procedures for fear conditioning and extinction tests were described in a previous study (Zhang et al., 2016). On day 1 (the conditioning phase), mice were introduced into an illuminated conditioning chamber (24 × 24 × 30, L × W × H cm) with a metal fence floor and allowed to explore freely for two minutes. Auditory tones (20 s, 7.5 kHz, sine wave, 80-90 dB) were coupled to scrambled footshocks (1 s, 0.7 mA; Beijing TMHY); both stimuli were co-terminated. Inter-tone intervals were randomly set between 60 and 120 s. Five conditioning trials were applied. On days 2-4 (the test phase), mice were introduced into an illuminated conditioning chamber (40 × 30 × 30, L × W × H cm) which contained plexiglas walls and a white filter paper on the floor. Ten auditory tones (20 s, 7.5 kHz, sine wave, 80-90 dB) were delivered after 3-min habituation. The inter-tone intervals were randomly set between 60 and 120 s. Mice were returned to their home cages 3 min after the end of last tone.

All behaviors were recorded with a camera above the apparatus. The mouse behavior was manually scored offline: ‘‘freezing’’ behavior was defined as the absence of movement, except for those related to respiration and slight head tremble. Freezing

behaviors which lasting less than one second were filtered out. For optogenetic inhibition of DRN DA neurons, blue laser pulses (473 nm, 20 s, 3-5 mW at the fiber tip) was delivered simultaneously during auditory tone delivery.

Pain threshold test

The procedures for pain threshold test were described in detail in previous studies (Soria-Gómez et al., 2015; Zhang et al., 2016). Mice were individually placed into the fear-conditioning chamber as described above. After two minutes of free exploration, the mouse received three repeated scrambled foot shocks with various intensities (e.g., 0.05, 0.1, 0.2, 0.3, 0.4, 0.5, and 0.6 mA). The shock lasted 1 s, and the inter-shock intervals were at least 1 min. The shock intensities at which the first vocalization and jumping event occurred were recorded and assigned as the vocalization and jumping thresholds accordingly. Once both of the thresholds for vocalization and jumping were determined, the test was terminated. The fear-conditioning chamber was completely cleaned between each mouse using ethanol and blown dry.

Morphine-induced CPP test

We used the custom-made three-compartment CPP apparatus described above for this test. On day 1 (the pretest phase), mice were allowed to freely explore the CPP apparatus for 30 min to assess their baseline place preferences. Any mouse that exhibited a strong initial preference for one of the side chambers (greater than 4.5-min difference) was pretested again until the strong initial preference was reduced. On days 2-5 (conditioning phase), pairings were performed. Daily conditioning consisted of two 30-min sessions with a 6-h interval: (1) the initially less preferred side was paired with morphine; (2) the initially preferred side was paired with saline. For each session, mice received an i.p. injection of either saline or morphine (10 mg/kg) and were confined to the assigned chamber for 30 min. The injection sequence was alternated on successive days. On day 6 (the test phase), mice were again allowed to freely explore the CPP apparatus for 30 min, as on day 1. For the experiments shown in Figures S4D and S4E, four additional extinction tests were performed on days 7-10. In the extinction tests, mice were also allowed to freely explore the CPP apparatus for 30 min, as on day 1 and day 6.

For optogenetic inhibition of DRN DA neurons in the conditioning phase, blue laser pulses (473 nm; 3-5 mW at the fiber tip; 5 s on, 5 s off) were delivered during morphine sessions. For optogenetic activation of DRN DA neurons in the conditioning phase, blue laser pulses (473 nm; one train of 8 pulses per second, 5 ms pulse width, 30Hz; according to Matthews et al., 2016) were delivered during morphine sessions. For optogenetic inhibition DRN DA neurons in the test phase, constant blue laser light (473 nm; 3-5 mW at the fiber tip) was delivered when mice were in the morphine-paired chamber. To minimize potential tissue damage, the laser was turned off temporarily for 15 s if it had been on continuously for 30 s. For optogenetic inhibition of VTA DA neurons in the conditioning phase, blue laser pulses (473 nm; 3-5 mW at the fiber tip; 5 s on, 5 s off) were delivered during both saline and morphine sessions. For optogenetic inhibition of VTA DA neurons in the test phase, constant blue laser light (473 nm; 3-5 mW at the fiber tip; 5 s on, 5 s off) was delivered. For axon terminal inhibition of DRN-projecting LPB neurons in the DRN using DREADDS during the conditioning phase, 200 nL CNO (30 μM; HB6149, HelloBio) or ACSF were infused into the DRN through cannula (100 nL/min) 15 min before the morphine or saline sessions, respectively. For axon terminal inhibition of DRN-projecting LPB neurons in the DRN during the test phase, 200 nL CNO were infused into the DRN through cannula 15 min before the test. Animal behaviors were tracked and analyzed as described above. The CPP score was calculated by subtracting the ratio of time spent in saline-paired chamber from the ratio of time spent in morphine-paired chamber. The ΔCPP score was calculated as the difference between the initial CPP score in the pretest and the CPP score in the test phase.

Spontaneous morphine withdrawal-induced conditioned place aversion (CPA) test

We adopted previously described procedures for this test (Bechara et al., 1995; Zhu et al., 2016). The custom-made three-compartment CPP apparatus was used. On day 1 (the pretest phase), mice were allowed to freely explore the CPP apparatus for 15 min to assess their baseline place preferences. Any mouse that exhibited a strong initial preference for one of the side chambers (greater than 2.25-min difference) was pretested again until the strong initial preference was reduced. On days 2-5 (the conditioning phase), mice received daily i.p. injections of morphine (20 mg/kg) in their home cages. Sixteen hours after each morphine injection, mice were confined for 45 min in the initially preferred chamber. On day 6 (the test phase), mice were again allowed to freely explore the CPP apparatus for 15 min, as on day 1. For the experiments shown in Figure S9A, an additional test was performed on day 12, in which mice were also allowed to freely explore the CPP apparatus for 15 min as on day 1 and day 6.

For optogenetic inhibition in both the conditioning and test phases, blue laser pulses (473 nm; 3-5 mW at the fiber tip; 5 s on, 5 s off) were delivered. Animal behaviors were tracked and analyzed as described above. The CPA score was calculated via subtracting the ratio of time spent in initially less preferred side from the ratio of time spent in initially preferred side. The ΔCPA score was calculated as the difference between the CPA score in the pretest and the score in the test phase.

Naloxone-precipitated morphine withdrawal-induced CPA test

Naloxone-precipitated morphine withdrawal-induced CPA test was performed according to a previous study (Zhu et al., 2016). The custom-made three-compartment CPP apparatus described above was used for this test. On day 1 (the pretest phase), mice were allowed to freely explore the CPP apparatus for 15 min to assess their baseline place preference. Any mouse that exhibited a strong initial preference for one of the side chambers (greater than 2.25-min difference) was pretested again until the strong initial preference was reduced. On the 6 consecutive days (days 1-6), mice received daily i.p. injections of morphine with increasing doses of 10, 20, 30, 40, 50, and 50 mg/kg in their home cages. Two hours after the last morphine injection, individual mice received an i.p. injection of naloxone (5 mg/kg) and were confined in the initially preferred side of the CPP apparatus for 20 min. Withdrawal symptoms were recorded. Physical signs (jumping, rearing, and tremor) were manually quantified offline. On day 7 (the test phase), mice were again

allowed to freely explore the CPP apparatus for 15 min, as on day 1. For the experiments shown in Figure S9B, an additional test was performed on day 13, in which mice were also allowed to freely explore the CPP apparatus for 15 min as on day 1 and day 7. The CPA score and the ΔCPA score were calculated as described above.

Sensory detection of food

Mice were deprived of food for 24 h before tests. Mice were introduced into a chamber (20 × 20 × 22, L × W × H in cm) that had a plastic floor with a small hole in one corner. Under the floor, a Petri dish containing HFF chow was placed in the corner with the hole. Mice were allowed to freely explore the chamber, and behaviors were recorded using an overhead infrared camera. Video recordings were manually scored to identify sniffing bout.

HFF consumption

The recordings were conducted under two different conditions: (1) food deprivation for 24 h or (2) food *ad libitum*. On the recording day, mice were introduced into a chamber (20 × 20 × 22, L × W × H in cm). After 2-min habituation, ten HFF pellets (12 mg/pellet, Bio-serv) were manually delivered to a small platform (3.5 cm diameter, 1 cm height) in one corner of the chamber. The interval between each pellet delivery was 1 min. Mouse behaviors were recorded using an overhead infrared camera. Video recordings were manually scored to identify eating bouts.

Fear conditioning and extinction test for fiber photometry

On day 1 (the conditioning phase), mice were introduced into a white acrylic box (24 × 24 × 30, L × W × H in cm) with a floor of metal fencing and allowed to explore freely for 2 min. 30 trials that consisted of footshocks (0.7 mA scrambled, 0.5 s) delivered after an auditory tone (2 s, 12 kHz, 80-90 dB) with a 1 s delay were then conducted. Inter-trial intervals were randomly set between 30-50 s. On day 2 (the extinction phase), mice were introduced into a test chamber (24 × 24 × 30, L × W × H cm) that had transparent plexiglas walls and a white filter paper as the floor. 20 auditory tones (same as the auditory tone for conditioning) were delivered after 2-min habituation without any footshock. The inter-tone intervals were randomly set between 30-50 s. Auditory tone onset was used as the trigger event for data alignment.

Juvenile intruder mice

The recording was conducted according to the previous study (Matthews et al., 2016). Mice were singly housed for at least one week. The recording was performed in mice's home cages. After 2-min habituation, a juvenile mouse was introduced into the home cage. The recording lasted for 5 min. Bouts of interaction with the juvenile intruder were scored manually.

Appetitive classical conditioning

Appetitive classical conditioning was performed as previously described (Zhong et al., 2017), with minor modifications. Mice were deprived of water for 24 h before training. On days 1-5, daily conditioning sessions were conducted. In each of the conditioning sessions, mice were repetitively presented with 50 trials of cue-sucrose 'pairs' as follows: a 2 s tone (2 s, 4 kHz, 80-90 dB) followed by a 2 s delay and then the delivery of a 1 s sucrose solution (5% w/v), with 20-40 s randomized inter-trial intervals. The sucrose solution was delivered via a peristaltic pump into the oral cavity through an intraoral cheek fistula. All behaviors were recorded with a camera above the apparatus. The speed of the mouse was calculated every 0.4 s from the video recording data using a custom MATLAB program. On day 6, five different delivery times of sucrose solution (e.g., 0, 0.5, 1, 2, and 5 s) were used to examine the effects of reward sizes. For each reward size, 8 trials were performed. Trials with different reward sizes were presented in random sequences.

Morphine-induced CPP test for fiber photometry

The morphine-induced CPP test was performed as described above. During the conditioning phase (days 2-5), mice received daily i.p. injection of saline or morphine (10 mg/kg). On the test day (day 6), mice were first confined in one chamber and recorded for 30 min. After this initial recording, mice were returned to their home cage. 2 h later, mice were confined in another chamber and again recorded for 30 min. Ca^{2+} transients were identified using previously described methods (Gunaydin et al., 2014).

Spontaneous morphine withdrawal-induced CPA test for fiber photometry

The spontaneous morphine withdrawal-induced CPA test was conducted as described above. On day 1, the activity of DRN DA neurons was recorded during the 15-min pretest. On days 1-4, mice received daily i.p. injection of saline or morphine (20 mg/kg) in their home cage and were conditioned with the initially preferred chamber 16 h after each injection. On day 5, mice were allowed to freely explore the CPP apparatus and were recorded for 15 min. Mouse behaviors were recorded using an overhead infrared camera. Animal behaviors were tracked and analyzed as described above. Ca^{2+} transients were identified using previously described methods (Gunaydin et al., 2014).

Fiber photometry

Fiber photometry was performed using a previously described system (Zhong et al., 2017). The GCaMP or DA signals were recorded during entire behavior tasks. The analog voltage signals were digitalized at 100 Hz and recorded using a custom script written in LabView.

Testing behavioral effects on Fos expression

To examine the behavioral effects on Fos expression patterns, behavior tasks were conducted as described above with minor modifications. To detect the expression of Fos during the conditioning phase of the morphine-induced CPP test, mice were i.p. injected with morphine or saline (10 mg/kg) and confined in the assigned chamber for 30 min on the day after the pretest. To detect the expression of Fos during the test phase of HFF and morphine-induced CPP, mice were confined in one paired chamber for 30 min on the test day. To detect the expression of Fos during the conditioning phase of the spontaneous morphine withdrawal-induced CPA test, mice

were i.p. injected with morphine (20 mg/kg) in their home cages. 16 h later, mice were confined for 45 min in the assigned chamber. To detect the expression of Fos during the test phase of the spontaneous morphine withdrawal test, mice were first injected and conditioned with saline and morphine (20 mg/kg). On the test day, mice were allowed to freely explore the CPP apparatus for 15 min. To detect the expression of Fos during footshock, 5 footshocks (1 s, 0.7 mA) were delivered with the inter-trial interval set randomly between 60 s and 120 s. Mice were returned to their home cage after behavior tasks. 30 min later, mice were deeply anaesthetized and perfused.

Patch-clamp electrophysiology

Mice were anesthetized with an overdose of pentobarbital (100 mg/kg, i.p.) and then transcardially perfused with ice-cold oxygenated slicing solution (5 mL, 0.5 mL/s). The slicing solution contained the following (mM): 110 choline chloride, 2.5 KCl, 0.5 $CaCl_2$, 7 $MgCl_2$, 1.3 NaH_2PO_4, 25 $NaHCO_3$, 10 glucose, 1.3 Na-ascorbate, and 0.6 Na-pyruvate. After perfusion, the mouse brain was dissected out and placed into ice-cold oxygenated slicing solution. Sections containing the DRN or the LPB (200 μm) were cut with a vibratome (VT1200s, Leica). The slices were incubated for 1 h at 34°C in oxygenated artificial cerebrospinal fluid (ACSF) that contained the following (mM): 125 NaCl, 2.5 KCl, 2 $CaCl_2$, 1.3 $MgCl_2$, 1.3 NaH_2PO_4, 1.3 Na-ascorbate, 0.6 Na-pyruvate, 10 glucose, and 25 $NaHCO_3$. The brain slices were transferred to a recording chamber at room temperature for recordings and imaging. All chemicals used in the slice preparation were purchased from Sigma.

Slices were submerged and superfused with ACSF at a rate of 2 mL/min at room temperature. Neurons were identified with differential interference contrast optics (DIC; Olympus BX51WI). The pipettes (3-4 MΩ) used for the recordings were prepared using a micropipette puller (P1000, Sutter Instrument). For whole-cell recordings, the pipettes were filled with an internal solution that contained the following (mM): 130 K-gluconate, 10 HEPES, 0.6 EGTA, 5 KCl, 3 Na_2ATP, 0.3 Na_3GTP, 4 $MgCl_2$, and 10 Na_2-phosphocreatine (pH 7.2–7.4). Voltage- and current-clamp recordings were performed with a MultiClamp 700B amplifier (Molecular Devices). The neurons were held at −65 mV. The traces were low-pass filtered at 3 kHz and digitized at 10 kHz (DigiData 1440, Molecular Devices). Data were acquired and analyzed using Clampfit 10.0 software (Molecular Devices).

For photostimulation, an optical fiber (200 μm core diameter, NA = 0.22) coupled to a diode-pumped solid-state 473 nm laser was submerged in ACSF and placed ~300 μm from the recording site. Delivery of optical laser was controlled by a laser driver (VD-IIA DPSS) and digital commands from the DigiData 1440 digitizer. Blue laser pulses lasting 5 s or 30 s were used to verify the efficiency of GtACR1 inhibition. A single brief pulse (5 ms) was used to elicit excitatory postsynaptic currents (EPSCs) and ten sweeps of EPSCs were averaged for each data point. The amplitudes of EPSCs were measured by subtracting the peak with the mean of the baseline before the stimulation. Tetrodotoxin (TTX, 1 μM; Sigma), a voltage-gated sodium channel antagonist, and 4-aminopyridine (4-AP, 1 mM; Sigma), a potassium channel antagonist, were added to isolate monosynaptic connections and 6, 7-dinitroquinoxaline-2, 3-dione (DNQX, 20 μM; Sigma) was added to block AMPA receptors.

For analysis of the LPB neuron excitability, currents were injected from −100 to 180 pA (with a step increase of 20 pA). The frequency of action potential firing was measured for each depolarizing current step and was plotted against the magnitude of the injected current step.

Rabies screen

Rabies screen was performed according to a previous study (Beier et al., 2017). On day 1, we injected 250 nL of a 1:2 volume mixture of AAV-DIO-TVA-mCherry and AAV-DIO-G into the DRN of DAT-Cre mice. On days 17-20, mice received daily i.p. injections of saline or morphine (10 mg/kg) in their home cages. On day 21, 500 nL RV*dG*-GFP was injected into the DRN of these same mice.

To inhibit DRN-projecting LPB neurons after RV infection, nine days before RV helper viruses injection, 100 nL AAVretro-FLPo were injected into the DRN and 30 nL AAV2-hEF1a-fDIO-hM4D(Gi)-mCherry-WPRE-pA or AAV2-EF1a-fDIO-H2B-mCherry were injected bilaterally into the LPB. After RV injection, mice were provided with drinking water containing CNO (5 mg/kg/day) and saccharin (5 mM, Sigma).

One week after rabies injection, mice were sacrificed and perfused. After PFA fixation and sucrose dehydration, consecutive 50 μm coronal sections of the whole brain were prepared on a cryostat (CM1900, Leica). The sections were imaged using the Olympus VS120 virtual microscopy slide scanning system with a 10 × objective. Cell counting was performed manually using Fiji (NIH).

Immunohistochemistry

Mice were anesthetized with an overdose of pentobarbital and perfused intracardially with phosphate-buffered saline (PBS), followed by paraformaldehyde (PFA, 4% wt/vol in PBS). Brains were removed and postfixed in 4% PFA for 4 h at room temperature. Samples were dehydrated in 30% sucrose solution. Thin sections (30-50 μm) were prepared on a cryostat microtome (Leica CM1950). Samples were permeabilized in PBS with 0.3% Triton X-100 (PBST) and blocked in 2% BSA in PBST at room temperature for 1 h. Sections were then incubated with primary antibodies (anti-TH, 1:1000, AB152, Millipore; anti-TH, 1:1000, ab76442, Abcam; anti-c-Fos, 1:2000, 2250, Cell Signaling Technology; anti-GFP, 1:1000, A10259, Thermo Fisher Scientific; or anti-HA, 1:1000, 11815016001, Roche) at 4°C. Samples were washed three times in PBST and were then incubated with fluorescent secondary antibodies (goat anti-rabbit Cy3, 1:500, 111-165-144, Jackson ImmunoResearch Labs; goat anti-chicken Alexa Fluor 488, 1:500, 703-545-155, Jackson ImmunoResearch Labs; or goat anti-rat Cy3, 1:1000, A10522, Thermo Fisher Scientific) at room temperature for 2 h. Samples were then washed three times in PBST. Counting of Fos^+ and TH^+ cells was performed manually using the Fiji program.

QUANTIFICATION AND STATISTICAL ANALYSIS

We used MATLAB R2014b and GraphPad Prism 6 to perform the statistical analysis. Sample sizes (n) usually denote the experimental replications as reported in the figure legends. In all behavioral experiments, sample sizes (n) denote the number of mice used. In slice recording experiments, sample sizes (n) denote the cell numbers recorded. Data were reported as means ± SEM in all figures. The exact *P value*s and the corresponding inferential statistical methods are stated in figure captions and legends. Detailed statistical tests are provided in Table S2. The values for the area under the Z-score curve were calculated using the function "trapz" in MATLAB.

DATA AND CODE AVAILABILITY

Data and custom programs are available upon request.

Neuron, Volume *106*

Supplemental Information

The Raphe Dopamine System Controls the Expression of Incentive Memory

Rui Lin, Jingwen Liang, Ruiyu Wang, Ting Yan, Youtong Zhou, Yang Liu, Qiru Feng, Fangmiao Sun, Yulong Li, Anan Li, Hui Gong, and Minmin Luo

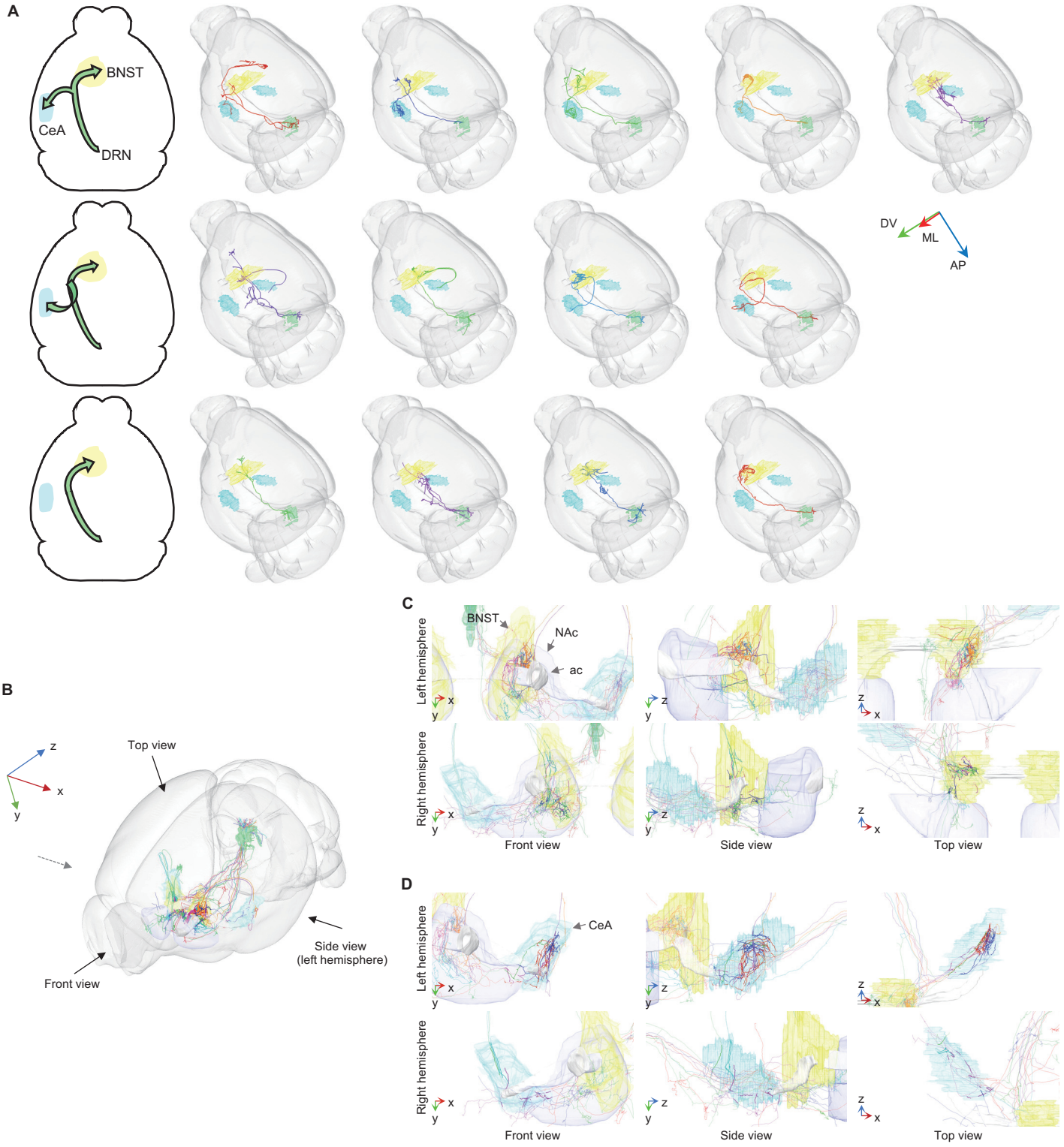

Figure S1. Whole-brain reconstruction of individual dorsal raphe (DRN) dopamine (DA) neurons, Related to Figure 1.

(**A**) Example views of the reconstructed individual DRN DA neurons registered in the reference brain.

(**B**) Schematics of camera angles for the front, side, and top views.

(**C**) Reconstructions of the axons of DRN DA neurons. Thickened lines represent axons located in the BNST. Each color represents a single cell.

(**D**) Reconstructions of the axons of DRN DA neurons. Thickened lines represent axons located in the CeA. Each color represents a single cell.

BNST: bed nucleus of the stria terminalis; CeA: central amygdala; NAc: Nucleus accumbens; ac: anterior commissure. Scale bar, 200 μm.

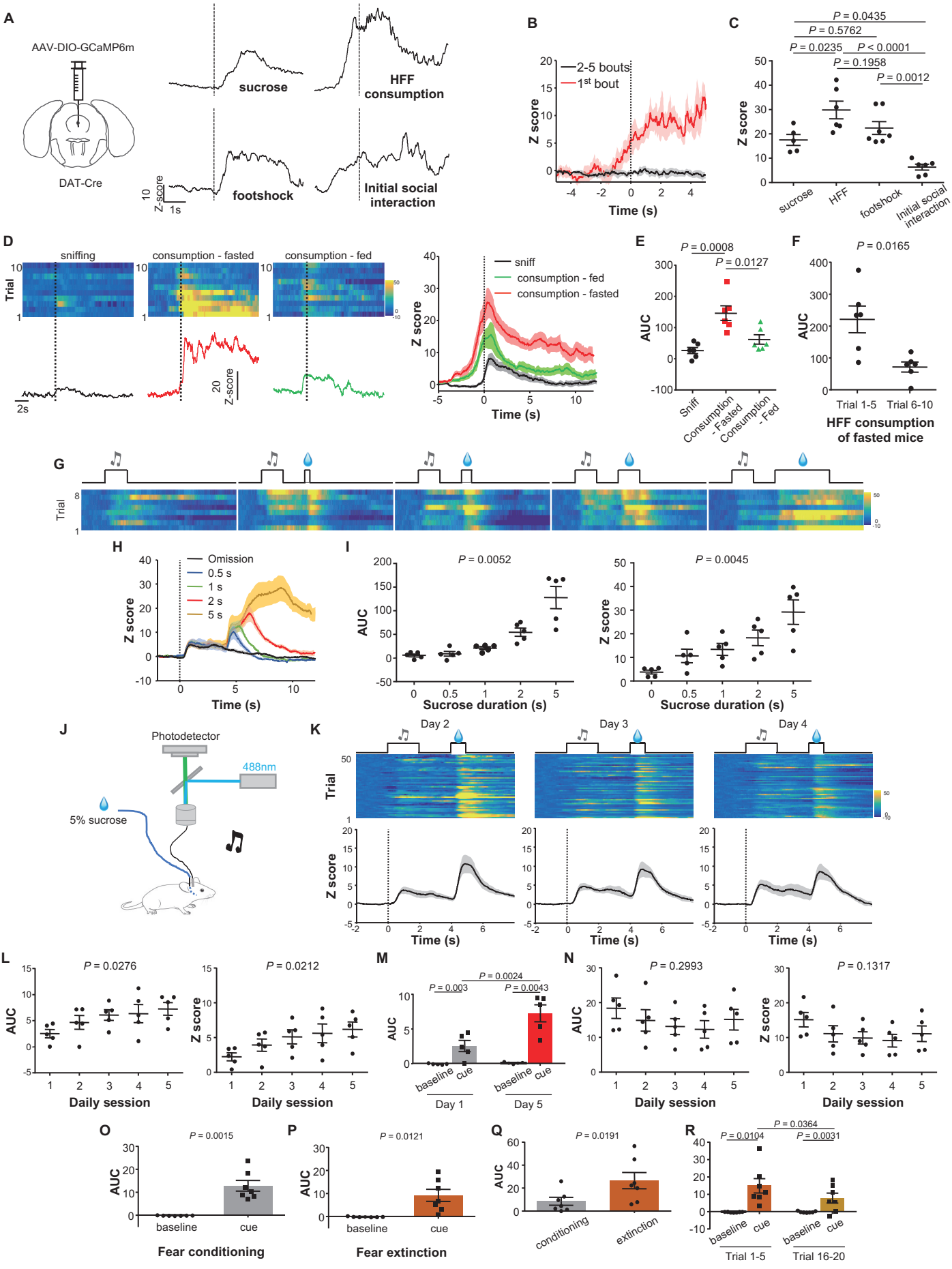

Figure S2 legend in the next page

Figure S2. DRN DA neurons are activated by both rewarding and aversive stimuli, and the response patterns are shaped by learning, Related to Figure 2.

(**A**) Fiber photometry of Ca^{2+} signals of DRN DA neurons in responses to various stimuli. The right panel shows raw traces of Ca^{2+} signals aligned to the initiation of sucrose delivery, high fat food (HFF) consumption, footshock, and the first bout of social interaction.

(**B**) Population Z score plots showing the averaged response to juvenile intruder mice in the first and 2-5 interaction bouts (n = 6 mice).

(**C**) Comparison of the peak Z score of the average response to the consumption of sucrose, consumption of HFF pellets, footshock, and juvenile intruders (one-way ANOVA with *post hoc* Tukey's test; n = 5 mice for sucrose, 6 mice for HFF pellets, 7 mice for footshock, and 6 mice for juvenile intruders).

(**D**) Fiber photometry of DRN DA neurons during the detection and consumption of HFF pellets. Left: example heatmaps (upper) and raw traces (lower) of Ca^{2+} signal aligned to the initiation of sniffing or consuming HFF pellets. Right: peri-event plots of the average Ca^{2+} signals of DRN DA neurons during the detection and consumption of HFF pellets (n = 6 mice).

(**E**) Quantification of the area under curve (AUC) of the average response to the detection and consumption of HFF pellets (two-sided *t*-test corrected for multiple comparisons using the Holm-Sidak method; n = 6 mice).

(**F**) The AUC of the average response to the consumption of HFF pellets in fasted mice for the first 5 feeding bouts and the second 5 feeding bouts (two-sided paired *t*-test; n = 6 mice).

(**G**) Heatmaps illustrating the Ca^{2+} signal changes (Z score) of DRN DA neurons to sucrose of different sizes (durations from left to right: 0, 0.5, 1, 2, 5 s).

(**H**) Peri-event plots of the average Ca^{2+} signals of DRN DA neurons responding to sucrose of different sizes (n = 5 mice).

(**I**) The AUC (left) and peak Z score (right) of the average response to the sucrose delivery of different sizes (one-way ANOVA; n = 5 mice).

(**J**) Schematic of fiber photometry of DRN DA neurons from freely behaving mice engaged in an appetitive Pavlovian conditioning task that coupled sucrose delivery with an auditory cue.

(**K**) Heatmaps illustrating the Ca^{2+} signal changes (top, Z score), and peri-event plots (bottom) of the average Ca^{2+} signals of DRN DA neurons from the second to fourth daily conditioning sessions. Heatmaps show representative data from a $DRN^{GCaMP6m}$ mouse. Peri-event plots show average traces from 5 $DRN^{GCaMP6m}$ mice.

(**L**) The AUC (left) and peak Z score (right) of the average response to the cue presentation (0-2 s) across five daily conditioning sessions (one-way ANOVA; n = 5 mice).

(**M**) The AUC of the average response during the baseline (-2-0 s before cue) and the cue presentation (0-2 s) in the first and the fifth daily appetitive Pavlovian conditioning sessions (n = 5 mice).

(**N**) The AUC (left) and peak Z score (right) of the average response to the sucrose delivery (4-6 s) across five daily classical conditioning sessions (n = 5 mice; one-way ANOVA).

(**O**) The AUC of the average response during the baseline (-2-0 s) and the cue presentation (0-2 s) in tone-footshock conditioning (two-sided paired *t*-test; n = 7 mice).

(**P**) The AUC of the average response during the baseline (-2-0 s) and the cue presentation (0-2 s) in tone-footshock extinction (two-sided paired *t*-test; n = 7 mice).

(**Q**) The AUC of the average response to the cue presentation (0-2 s) in the first trial of the tone-footshock conditioning session and the extinction session (two-sided paired *t*-test; n = 7 mice).

(**R**) The AUC of the average response during the baseline (-2-0 s) and the cue presentation (0-2 s) in the first and the last five trials of tone-footshock extinction session (n = 7 mice).

See Table S2 for detailed statistical tests. *P* values are shown in the graph. Data are means ± SEM.

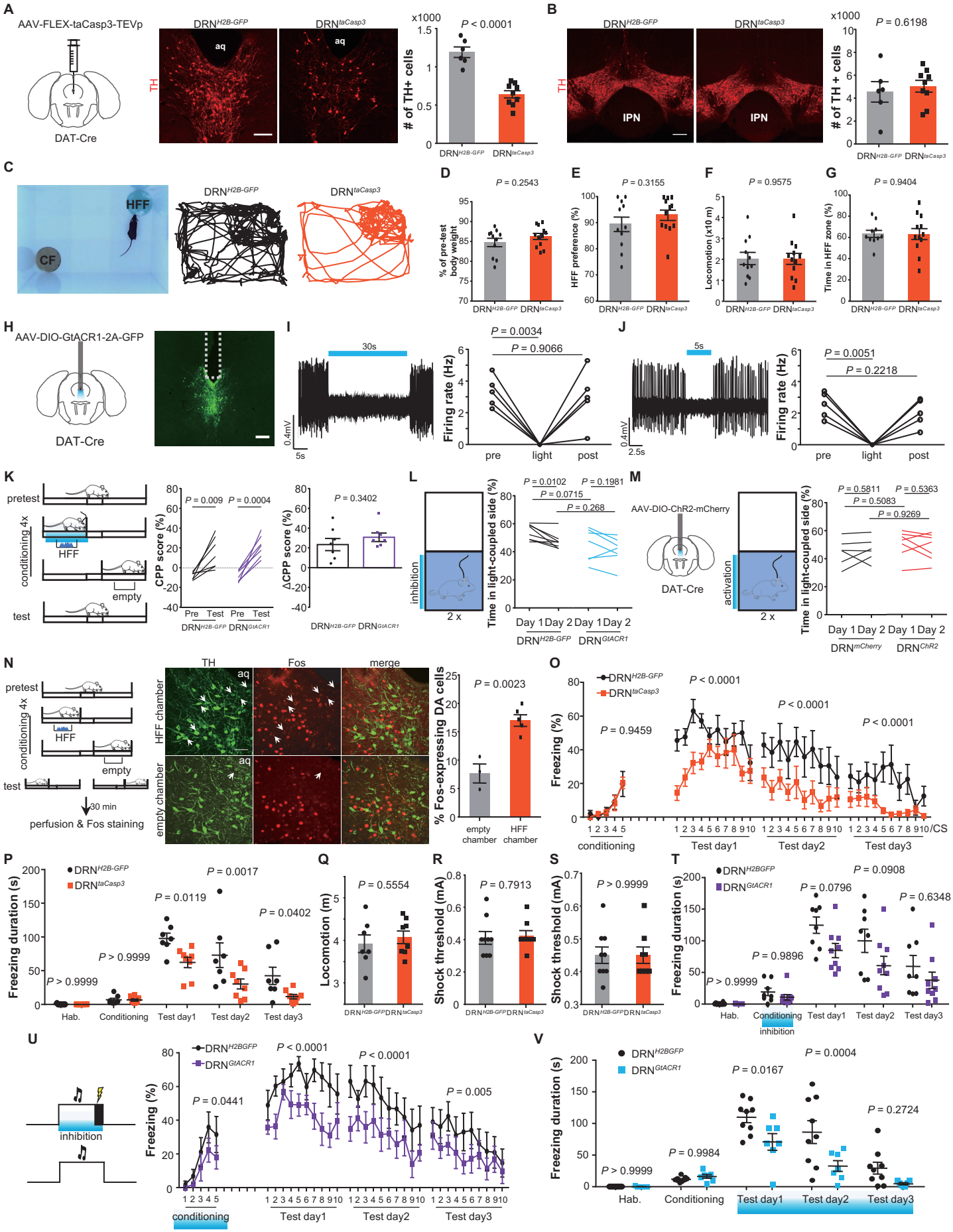

Figure S3 legend in the next page

Figure S3. DRN DA neurons are required for the expression of natural incentive memory, Related to Figure 2.

(**A**) The effect of genetically ablating DRN DA neurons on the number of tyrosine hydroxylase (TH)-positive neurons in the DRN of control (left) and lesion (right) mice (two-sided unpaired *t*-test; n = 6 $DRN^{H2B\text{-}GFP}$ mice in the ctrl group and 9 $DRN^{taCasp3}$ mice in the lesion group).

(**B**) TH expression in the VTA of control and DRN-lesioned mice (two-sided unpaired *t*-test; n = 6 $DRN^{H2B\text{-}GFP}$ mice in the ctrl group and 9 $DRN^{taCasp3}$ mice in the lesion group).

(**C**) Example image and tracks showing behaviors of control and lesion mice in the food preference test. CF: common food chow powders.

(**D**-**G**) Quantification of body weight (D), HFF preference (E), locomotion (F), and time spent (G) in the HFF zone of control and lesion mice in the food preference test (two-sided unpaired *t*-test; n = 11 $DRN^{H2B\text{-}GFP}$ mice in the ctrl group and 12 $DRN^{taCasp3}$ mice in the lesion group).

(**H**) AAV-DIO-GtACR1-2A-GFP was injected into the DRN. Dashed lines indicate optic fiber placement.

(**I** and **J**) The effects of 30-s (I) and 5-s (J) 5-s continuous blue light stimulation on the spontaneous activity of GtACR1-expressing DRN DA neurons in a slice preparation (one-way ANOVA with *post hoc* Tukey's test; n = 5 cells for both tests).

(**K**) The effect of optogenetically inhibiting DRN DA neurons in the conditioning phase on HFF-induced CPP (n = 7 $DRN^{H2B\text{-}GFP}$ mice in the ctrl group and 7 DRN^{GtACR1} mice in the inhibition group).

(**L**) Optogenetic inhibition of DRN DA neurons did not induce real-time aversion (n = 8 $DRN^{H2B\text{-}GFP}$ mice in the ctrl group and 7 DRN^{GtACR1} mice in the inhibition group).

(**M**) Optogenetic activation of DRN DA neurons did not induce real-time aversion (n = 6 $DRN^{H2B\text{-}GFP}$ mice in the ctrl group and 7 DRN^{ChR2} mice in the activation group)

(**N**) Fos expression in DRN DA neurons during the test phase of the HFF-induced CPP test. The right panel shows the quantification of Fos expression in DRN DA neurons during the test phase of the HFF-induced CPP test (two-sided unpaired *t*-test; n = 3 mice in the empty dish group and 5 mice in the HFF group).

(**O** and **P**) The effect of ablating DRN DA neurons on mice's real-time freezing ratio (O; two-way ANOVA) and overall freezing duration (P; two-way ANOVA with *post hoc* Sidak's test) in the fear conditioning test (n = 7 $DRN^{H2B\text{-}GFP}$ mice in the ctrl group and 8 $DRN^{taCasp3}$ mice in the lesion group).

(**Q**) Quantification of animals' locomotion during the habituation of the fear conditioning test as shown in (O) and (P) (two-sided unpaired *t*-test; n = 7 $DRN^{H2B\text{-}GFP}$ mice in the ctrl group and 8 $DRN^{taCasp3}$ mice in the lesion group).

(**R** and **S**) Quantification of shock threshold for vocalization (R) and shock threshold for jumping (S) of control and lesion mice in the pain threshold test (two-sided unpaired *t*-test; n = 9 $DRN^{H2B\text{-}GFP}$ mice in the ctrl group and 8 $DRN^{taCasp3}$ mice in the lesion group).

(**T** and **U**) The effect of optogenetically inhibiting DRN DA neurons during the conditioning phase on mice's overall freezing duration (T; two-way ANOVA with *post hoc* Sidak's test) and real-time freezing ratio (U; two-way ANOVA) in the fear conditioning test (n = 8 $DRN^{H2B\text{-}GFP}$ mice in the ctrl group and n = 9 DRN^{GtACR1} mice in the inhibition group).

(**V**) Overall freezing responses of the control and DRN DA neurons-inhibited mice to discrete tones across different phases of the cue-footshock conditioning test as shown in Fig. 2F (two-way ANOVA with *post hoc* Sidak's test; n = 9 $DRN^{H2B\text{-}GFP}$ mice in the ctrl group and n = 7 DRN^{GtACR1} mice in the inhibition group).

See Table S2 for detailed statistical tests. *P* values are shown in the graph. Data are means ± SEM. Scale bars, 200 μm (A and B), 100 μm (H), 50 μm (N).

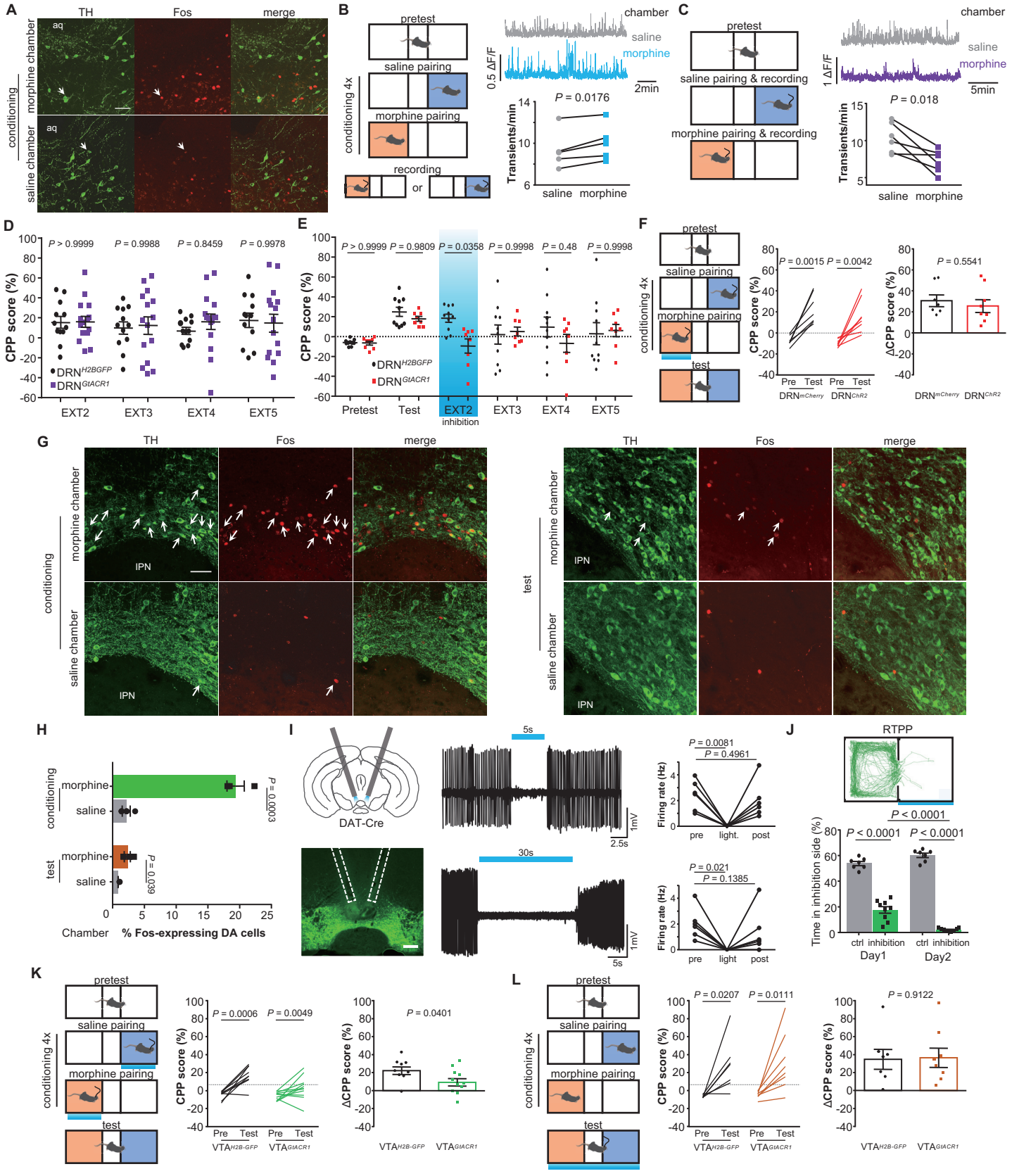

Figure S4 legend in the next page

Figure S4. DRN DA neurons are dispensable for the formation of morphine reward memory, Related to Figure 3.

(**A**) Fos expression in DRN in the conditioning phase of the morphine-induced CPP test.

(**B**) Ca^{2+} transient analysis of DRN DA neurons in the test phase of the morphine-induced CPP test (two-sided paired *t*-test; n = 5 mice).

(**C**) The effect of acute delivery of morphine or saline on the Ca^{2+} transients of DRN DA neurons in the conditioning phase of the morphine-induced CPP test (two-sided paired *t*-test; n = 6 mice).

(**D**) The effect of optogenetically inhibiting DRN DA neurons in the conditioning phase on the extinction of morphine-induced CPP (two-way ANOVA with *post hoc* Sidak's test; n = 12 $DRN^{H2B\text{-}GFP}$ mice in the ctrl group and 15 DRN^{GtACR1} mice in the inhibition group).

(**E**) The effect of optogenetically inhibiting DRN DA neurons in the second session of the conditioning phase on mice's performances in the morphine-induced CPP test (two-way ANOVA with *post hoc* Sidak's test; n = 10 $DRN^{H2B\text{-}GFP}$ mice in the ctrl group and 8 DRN^{GtACR1} mice in the inhibition group).

(**F**) The effect of optogenetically activating DRN DA neurons in the conditioning phase on morphine-induced CPP (n = 7 $DRN^{mCherry}$ mice in the ctrl group and 8 DRN^{ChR2} mice in the activation group).

(**G**) Fos expression in the VTA across different phases of the morphine-induced CPP test.

(**H**) Quantification of Fos expression in VTA DA neurons during the morphine-induced CPP test (two-sided unpaired *t*-test; n = 3 mice for each group).

(**I**) Optogenetic inhibition of VTA DA neurons using GtACR1. 5-s and 30-s continuous blue light stimulations effectively suppressed the spontaneous activity of VTA DA neurons (one-way ANOVA with *post hoc* Tukey's tests; n = 6 cells for both tests).

(**J**) Optogenetic inhibition of VTA DA neurons induced strong RTPA (n = 7 $VTA^{H2B\text{-}GFP}$ mice in the ctrl group and 9 VTA^{GtACR1} mice in the inhibition group).

(**K**) The effect of optogenetically inhibiting VTA DA neurons in the conditioning phase on morphine-induced CPP (n = 9 $VTA^{H2B\text{-}GFP}$ mice in the ctrl group and 11 VTA^{GtACR1} mice in the inhibition group).

(**L**) The effect of optogenetically inhibiting VTA DA neurons in the test phase on morphine-induced CPP (n = 7 $VTA^{H2B\text{-}GFP}$ mice in the ctrl group and 8 VTA^{GtACR1} mice in the inhibition group).

See Table S2 for detailed statistical tests. *P* values are shown in the graph. Data are means ± SEM. Scale bars, 50 μm.

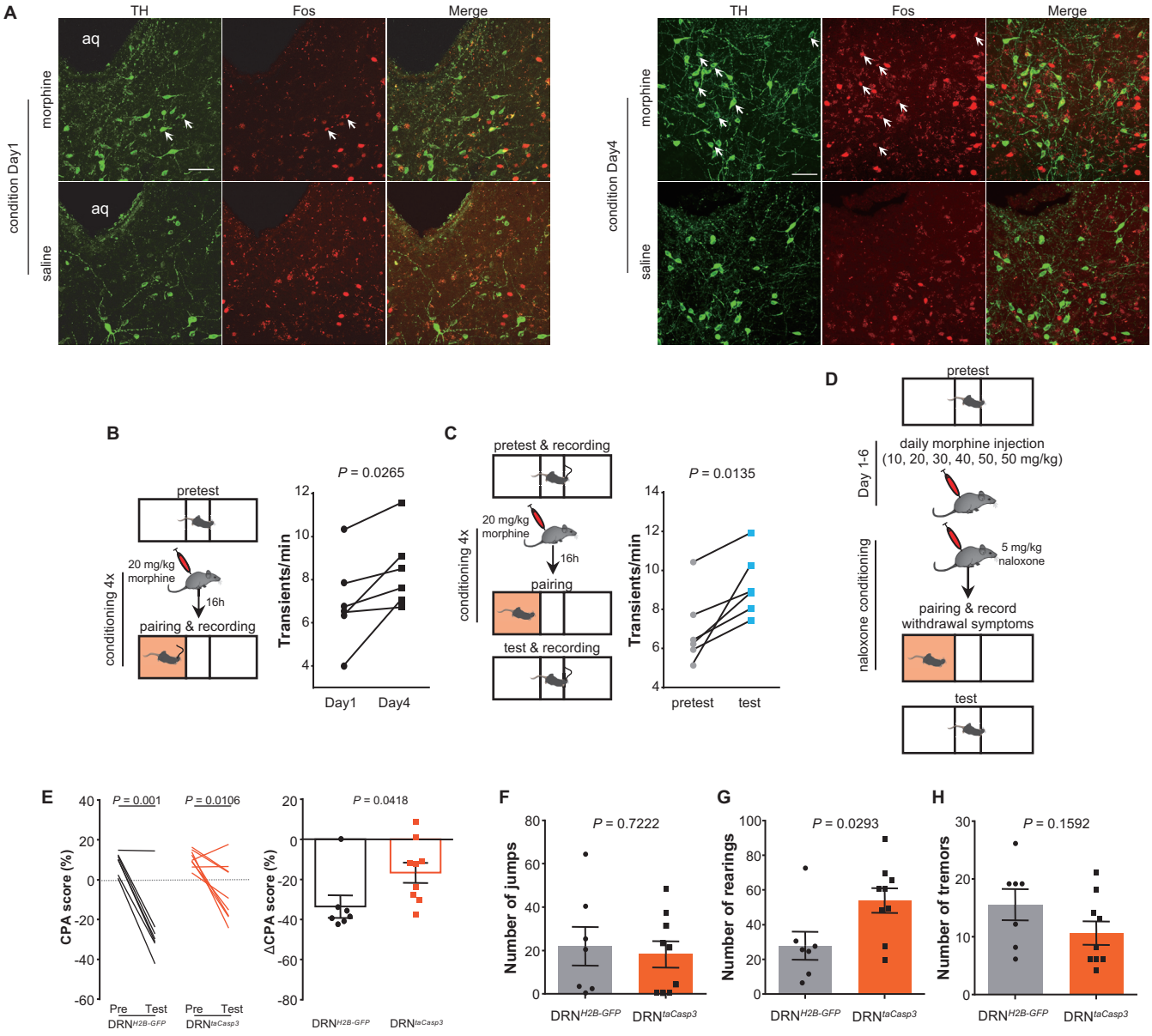

Figure S5. DRN DA neurons regulate the formation of opioid withdrawal memory, Related to Figure 4.

(**A**) Fos expression in the DRN in the first (left) and last (right) day of the conditioning phase of the spontaneous opioid withdrawal-induced CPA test.

(**B**) Ca^{2+} transient analysis of DRN DA neurons in first (Cond 1) and last (Cond 4) day of the conditioning phase of the spontaneous opioid withdrawal-induced CPA test (two-sided paired *t*-test; n = 6 mice).

(**C**) Ca^{2+} transient analysis of DRN DA neurons during the pretest and test phases of the spontaneous morphine withdrawal-induced CPA test (two-sided paired *t*-test; n = 6 mice).

(**D**) Schematic of the naloxone-precipitated opioid withdrawal induced CPA test.

(**E**) The effect of ablating DRN DA neurons on naloxone-precipitated opioid withdrawal induced CPA (two-sided unpaired *t*-test; n = 7 $DRN^{H2B\text{-}GFP}$ mice in the ctrl group and 9 $DRN^{taCasp3}$ mice in the lesion group).

(**F**-**H**) The effect of ablating DRN DA neurons on the expression of naloxone-precipitated withdrawal symptoms including jumps (F), rearings (G), and tremors (H) (two-sided unpaired *t*-test; n = 7 $DRN^{H2B\text{-}GFP}$ mice in the ctrl group and 9 $DRN^{taCasp3}$ mice in the lesion group).

See Table S2 for detailed statistical tests. *P* values are shown in the graph. Data are means ± SEM. Scale bars, 50 μm (A and B).

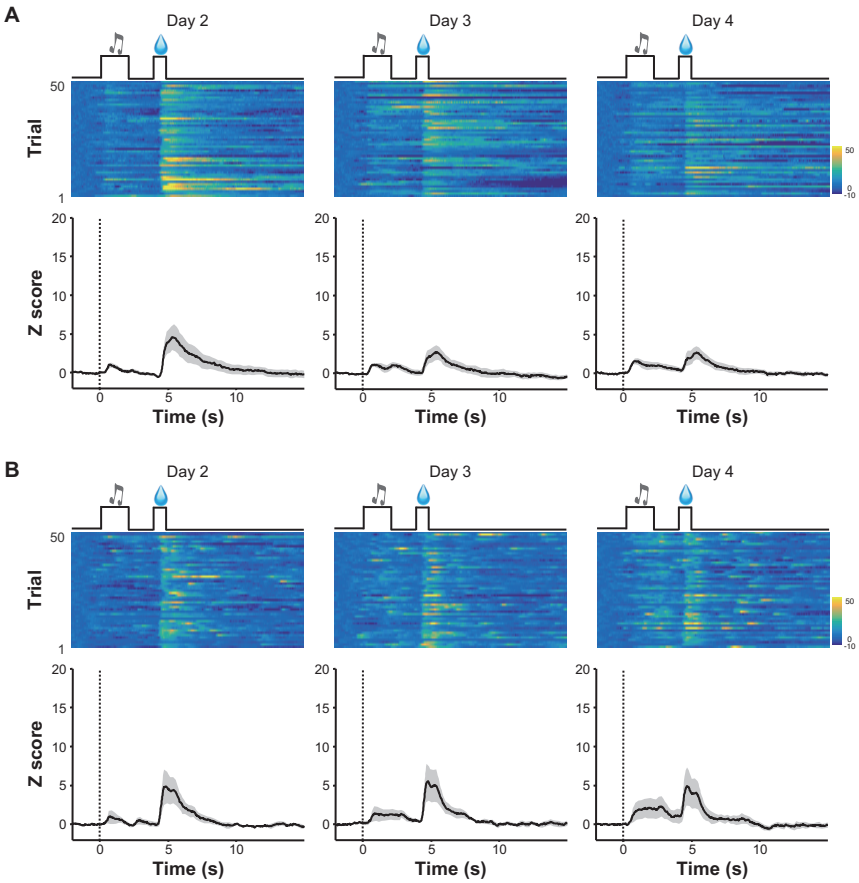

Figure S6. Learning shapes the DA release profile in the CeA and the BNST, Related to Figure 5.
(**A**) Heatmaps illustrating the DA signal changes (top, Z score), and peri-event plots (bottom) of the average DA signals in the CeA from the second to fourth daily conditioning sessions. Heatmaps show representative data from a recorded mouse. Peri-event plots show average traces from 8 recording sites in 6 mice.
(**B**) Heatmaps illustrating the DA signal changes (top, Z score), and peri-event plots (bottom) of the average DA signals in the BNST from the second to fourth daily conditioning sessions. Heatmaps show representative data from a recorded mouse. Peri-event plots show average traces from 4 mice.

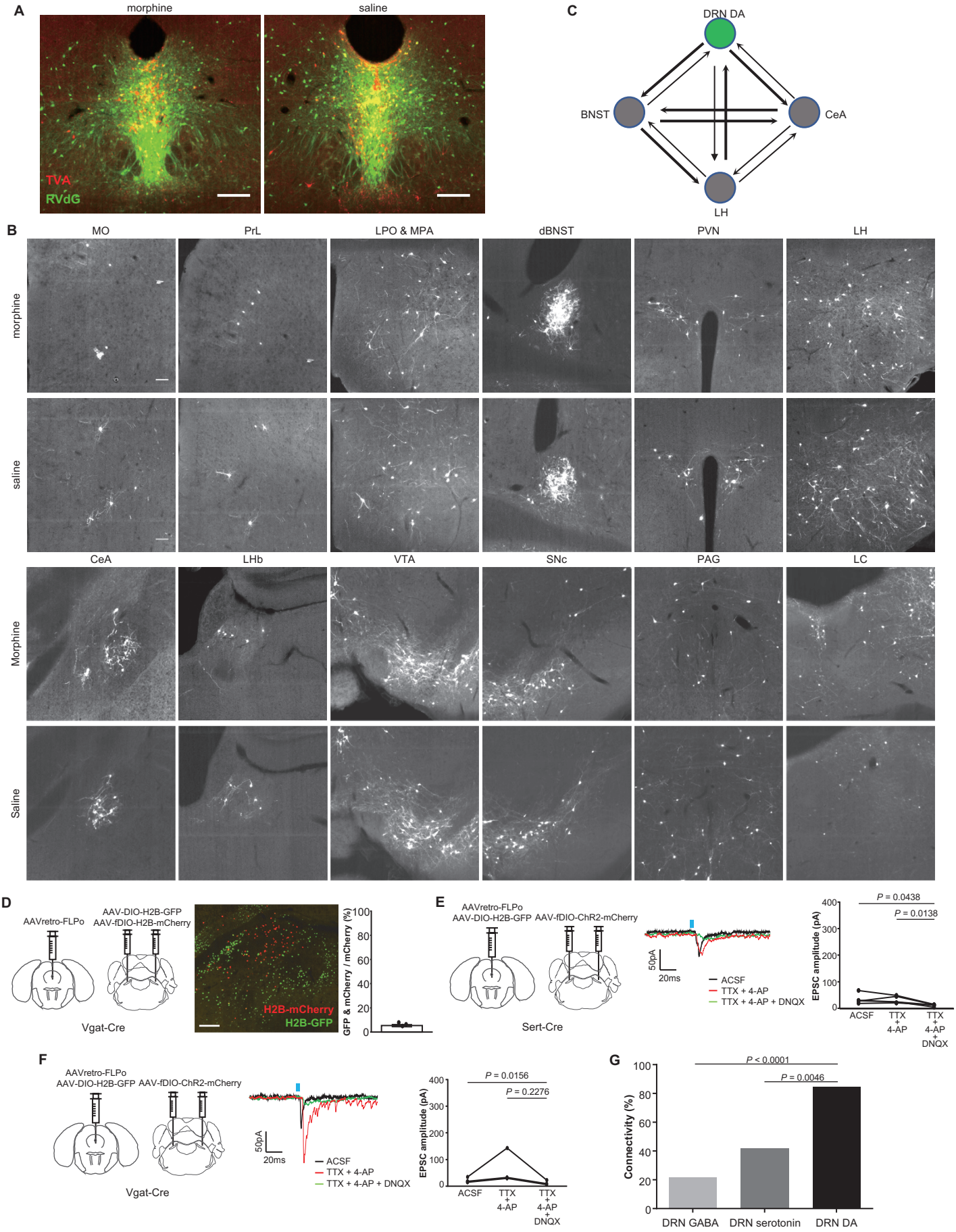

Figure S7 legend in the next page

Figure S7. Presynaptic partners of DRN DA neurons, Related to Figure 6.

(**A**) The distribution patterns of starter neurons (red) and RV-infected neurons (green) in the DRN of morphine- (left) and saline (right)-treated DAT-Cre mice.

(**B**) Coronal representation of retrograde monosynaptic labeling of input neurons to DRN DA neurons in the brains of morphine- (top) and saline (bottom)-treated mice. MO: medial orbital cortex; PrL: prelimbic cortex; LPO: lateral preoptic area; MPA: medial preoptic area; PVN: paraventricular nucleus; LHb: lateral habenula; SNc: substantia nigra pars compacta; PAG: periaqueductal gray; LC: locus coeruleus.

(**C**) Reciprocal connections between DRN DA neurons, BNST neurons, CeA neurons, and LH neurons.

(**D**) Overlay of dual-color labeled neurons in the LPB. DRN-projecting LPB neurons were labeled with H2B-mCherry (red). LPB GABAergic neurons were labeled with H2B-GFP (green) (n = 3 mice).

(**E**) The effect of optogenetically stimulating the axon terminals of LPB neurons in the DRN on DRN serotonin neurons (two-sided paired *t*-test; n = 5 cells). Left: schematic of virus injection. Middle: example traces of a recorded DRN serotonin neurons. ACSF: artificial cerebrospinal fluid; TTX: tetrodotoxin; 4-AP: 4-Aminopyridine; DNQX: 6,7-dinitroquinoxaline-2,3-dione.

(**F**) The effect of optogenetically stimulating the axon terminals of LPB neurons in the DRN on DRN GABAergic neurons (two-sided paired *t*-test; n = 3 cells). Left: schematic of virus injection. Middle: example traces of a recorded DRN GABAergic neurons.

(**G**) Quantification of the connectivity of DRN-projecting LPB neurons with DRN GABAergic neurons, DRN serotonin neurons, and DRN DA neurons (Chi-squared test; n = 3/14 for DRN GABAergic neurons, 5/12 for DRN serotonin neurons, and 27/32 for DRN DA neurons).

See Table S2 for detailed statistical tests. *P* values are shown in the graph. Scale bars, 100 μm (A and B), 200 μm (D).

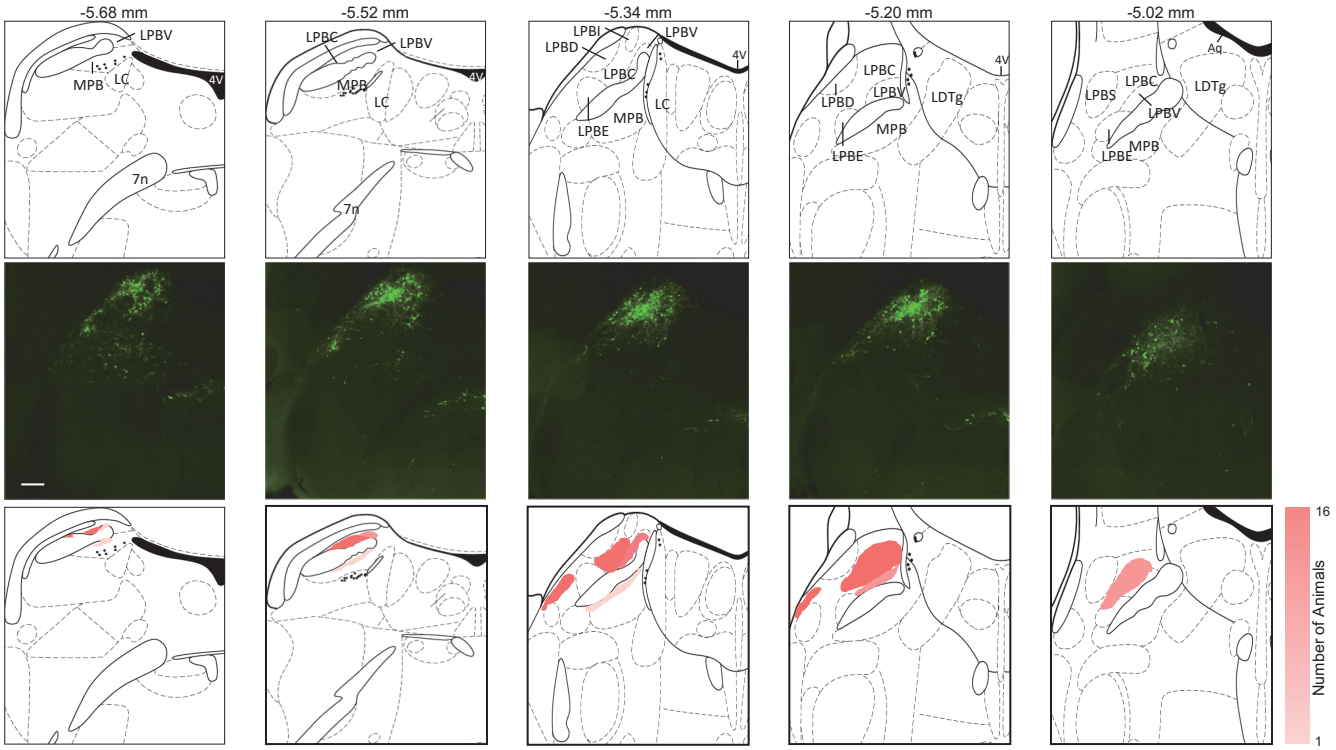

Figure S8. The distribution of DRN-projecting LPB neurons, Related to Figure 7.
The top panels illustrate the brain nuclei based on the mouse brain atlas by Paxinos and Franklin (2001), with numbers above the panels indicating the distance to Lamda. The middle panels show labeling from a representative mouse. The bottom panels show the overlay of TeNT expression in 16 mice, including 8 mice from the morphine-induced CPP test shown in Figure 7B and 8 mice from the spontaneous opioid withdrawal-induced CPA test shown in Figure S9A. The distance from the bregma is shown above the images. LPBC: central part of LPB; LPBD: dorsal part of LPB; LPBE: external part of LPB; LPBV: ventral part of LPB; LDTg: laterodorsal tegmental nucleus; MPB: medial parabrachial nucleus; 4V: 4th ventricle; 7n: facial nucleus. Scale bar, 100 μm.

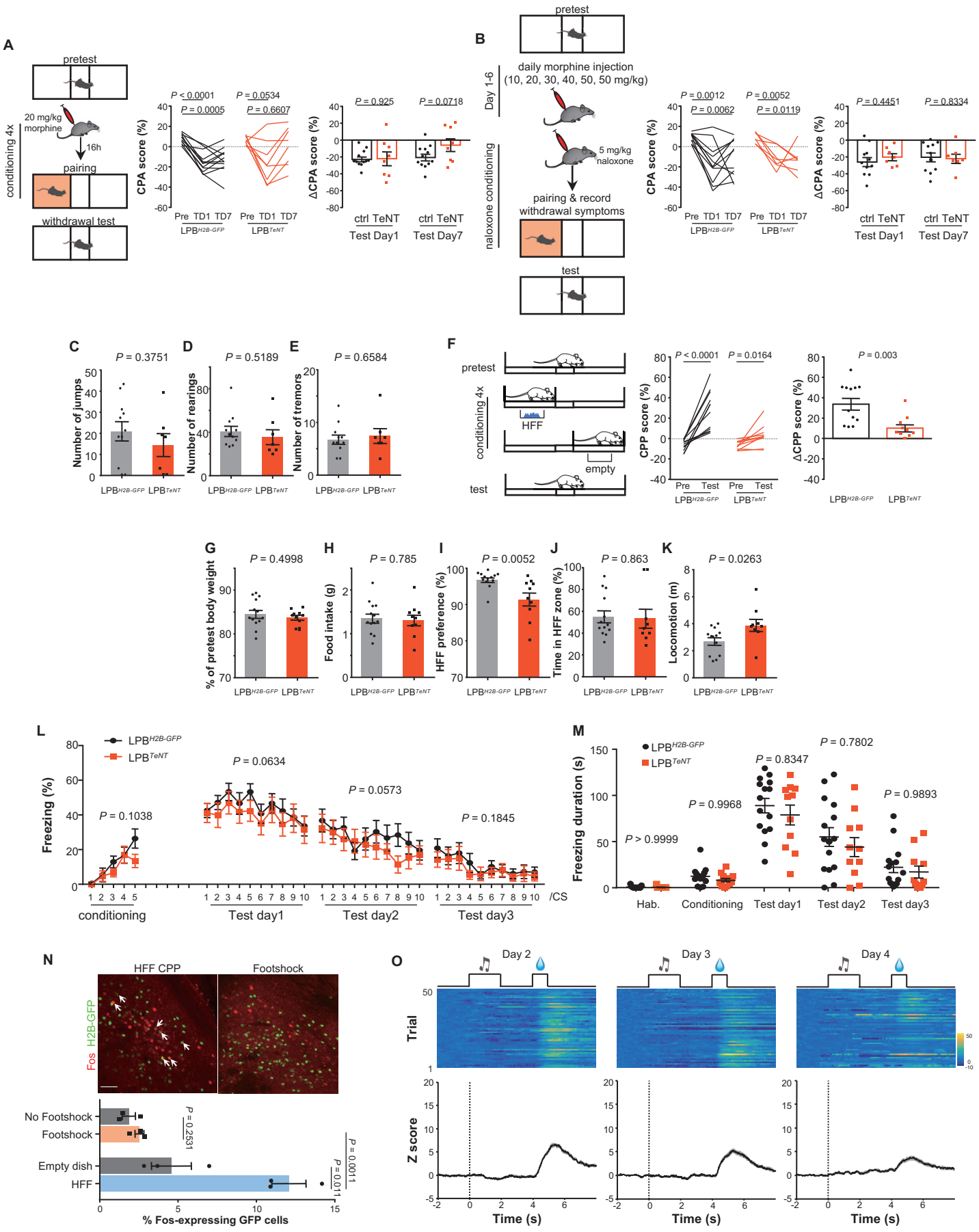

Figure S9 legend in the next page

Figure S9. DRN-projecting lateral parabrachial nucleus (LPB) neurons regulate reward processing, Related to Figure 7.

(**A**) The effects of blocking the neurotransmission of DRN-projecting LPB neurons on HFF-induced CPP (n = 12 $LPB^{H2B\text{-}GFP}$ mice in the ctrl group and 10 LPB^{TeNT} mice in the TeNT group).

(**B** and **C**) Blocking the LPB to DRN neurotransmission by expressing tetanus toxin (TeNT) in the DRN-projecting LPB neurons did not affect spontaneous opioid withdrawal-induced CPA (B; n = 12 $LPB^{H2B\text{-}GFP}$ mice in the ctrl group and 8 LPB^{TeNT} mice in the TeNT group) nor naloxone-precipitated opioid withdrawal-induced CPA (C; n = 11 $LPB^{H2B\text{-}GFP}$ mice in the ctrl group and 7 LPB^{TeNT} mice in the TeNT group).

(**D**-**F**) Quantification of jumps (D), rearings (E), and tremors (F) of mice in the control and the TeNT group in the naloxone-precipitated opioid withdrawal-induced CPA test (two-sided unpaired *t*-tests; n = 11 $LPB^{H2B\text{-}GFP}$ mice in the ctrl group and 7 LPB^{TeNT} mice in the TeNT group).

(**G**-**K**) Quantification of body weight (G), food intake (H), HFF preference (I), time in the HFF zone (J), and locomotion (K) of mice in the control and TeNT group in the food preference test (two-sided unpaired *t*-tests; n = 13 $LPB^{H2B\text{-}GFP}$ mice in the ctrl group and 10 LPB^{TeNT} mice in the TeNT group).

(**L** and **M**) Blocking the neurotransmission of DRN-projecting LPB neurons did not affect mice's real-time freezing ratio (L; two-way ANOVA) or overall freezing duration (M; two-way ANOVA with *post hoc* Sidak's test) in the fear conditioning test (n = 15 $LPB^{H2B\text{-}GFP}$ mice in the ctrl group and 11 LPB^{TeNT} mice in the TeNT group).

(**N**) Fos expression in the LPB in the test phase of the HFF-induced CPP test (top left) and in the fear conditioning test (top right). DRN-projecting LPB neurons were labeled with H2B-GFP. The bottom panel shows the quantification of Fos expression (two-sided unpaired *t*-test; n = 3 mice for each group).

(**O**) Heatmaps illustrating the Ca^{2+} signal changes (top, Z score), and peri-event plots (bottom) of the average Ca^{2+} signals of DRN DA neurons from the second to fourth daily conditioning sessions. Heatmaps show representative data from a recorded LPB^{TeNT} mouse. Peri-event plots show average traces from 5 mice.

See Table S2 for detailed statistical tests. *P* values are shown in the graph. Data are means ± SEM. Scale bar, 50 μm.

Table S1. Virus Injection, Related to STAR methods

Figure	Mice	Injection Site	Virus	Volume (nL)
Fig. 1B, C	DAT-Cre	DRN	AAV2-EF1a-DIO-mGFP	250
		VTA	AAV2-EF1a-DIO-mCherry	150 (bilateral)
Fig. 1D-F; Fig. S1	DAT-Cre	DRN	AAV2 -TRE-DIO-FLPo	150
			AAV2 -TRE-fDIO-GFP-IRES-tTA	(1:5 (v/v) mixture)
Fig. 2A-C; Fig. 7F-J; Fig. S2; Fig. S4B, C; Fig. S5B, C	DAT-Cre	DRN (fiber implantation)	AAV2-EF1a-DIO-GCaMP6m	250
Fig. 2D; Fig. 3C; Fig. 4C; Fig. S3A-G; Fig. S3O-S; Fig. S5D-H	DAT-Cre	DRN	ctrl group: AAV2-EF1a-DIO-H2B-GFP lesion group: AAV2-EF1a-FLEX-taCasp3-TEVp	200
Fig. 2E, F; Fig. 3D, E; Fig. 4D, E; Fig. S3H-L; Fig. S3T-V; Fig. S4D, E	DAT-Cre	DRN (fiber implantation)	ctrl group: AAV2-EF1a-DIO-H2B-GFP Inhibition group: AAV2-CAG-DIO-GtACR1-P2A-GFP	250
Fig. 5A-C; Fig. S6	C57BL/6N	CeA/BNST (fiber implantation)	AAV2-hSyn-GRAB$_{DA2m}$	200
Fig. 5E-I	C57BL/6N	DRN	ctrl group: AAV2-CMV-SaCas9-U6-sgRNA-GFP DRN-TH KO group: AAV2-CMV-SaCas9-U6-sgRNA-TH	150
Fig. 6A-C; Fig. S7A, B	DAT-Cre	DRN	AAV2-EF1a-DIO-TVA-mCherry	250
			AAV2-EF1a-DIO-RVG-WPRE-pA	(1:1 (v/v) mixture)
			RV*dG*-GFP	500
Fig. 6D	DAT-Cre	DRN	AAVretro-FLPo	100
			AAV2-EF1a-DIO-H2B-GFP	250
		LPB	AAV2-hEF1a-fDIO-hChR2(H134R)-mCherry-WPRE-pA	30 (bilateral)
Fig. 6E	C57BL/6N	DRN	AAVretro-Cre	100
		LPB	AAV2-EF1a-DIO-ChR2-mCherry	30 (bilateral)
Fig. 6F	DAT-Cre	DRN	AAVretro-FLPo	100
			AAV2-EF1a-DIO-TVA-mCherry	250
			AAV2-EF1a-DIO-RVG-WPRE-pA	(1:1 (v/v) mixture)
			RV*dG*-GFP	500
		LPB	AAV2-hEF1a-fDIO-H2B-mCherry or AAV2-hEF1a-fDIO-hM4D(Gi)-mCherry-WPRE-pA	30 (bilateral)
Fig. 7A-B; Fig. S8; Fig. S9A-M	C57BL/6N	DRN	AAVretro-Cre	100
		LPB	ctrl group: AAV2-EF1a-DIO-H2B-GFP TeNT group: AAV2-DIO-GFP-2A-TeNT	30 (bilateral)
Fig. 7C-E	C57BL/6N	DRN (cannula implantation)	AAVretro-FLPo	100
		LPB	ctrl group: AAV2-hEF1a-fDIO-H2B-	30 (bilateral)

			mCherry Inhibition group: AAV2-hEF1a-fDIO-hM4D(Gi)-mCherry-WPRE-pA	
Fig. 7F-L; Fig S9O	DAT-Cre	DRN (fiber implantation)	AAVretro-FLPo	100
			AAV2-EF1a-DIO-GCaMP6m	250
		LPB	Inhibition group: AAV2-EF1a-fDIO-mScarlet-2A-TeNT	30 (bilateral)
Fig. S3M; Fig. S4F	DAT-Cre	DRN (fiber implantation)	ctrl group: AAV2-EF1a-DIO-mCherry Activation group: AAV2-EF1a-DIO-ChR2-mCherry	200
Fig. S4I-L	DAT-Cre	VTA (fiber implantation)	ctrl group: AAV2-EF1a-DIO-H2B-GFP Inhibition group: AAV2-CAG-DIO-GtACR1-P2A-GFP	150 (bilateral)
Fig. S7D	Vgat-Cre	DRN	AAVretro-FLPo	100
		LPB	AAV2-fDIO-H2B-mCherry & AAV2-DIO-H2B-GFP	30 (bilateral)
Fig. S7E	Sert-Cre	DRN	AAVretro-FLPo	100
			AAV2-DIO-H2B-GFP	250
		LPB	AAV2-fDIO-ChR2-mCherry	30 (bilateral)
Fig. S7F	Vgat-Cre	DRN	AAVretro-FLPo	100
			AAV2-DIO-H2B-GFP	250
		LPB	AAV2-fDIO-ChR2-mCherry	30 (bilateral)
Fig. S9N	C57BL/6N	DRN	AAVretro-Cre	100
		LPB	AAV2-EF1a-DIO-H2B-GFP	30 (bilateral)